

STUDIES OF MAGMATIC SYSTEMS

by

Luca Fedele

Dissertation submitted to the Faculty of the
Virginia Polytechnic Institute and State University
in partial fulfillment of the requirements for the degree of
DOCTOR OF PHILOSOPHY

in

Geological Sciences

APPROVED:

R.J. Bodnar (Chairman)

B. DeVivo

H. Belkin

R.J. Tracy

J. Webster

J. Beard

May 9th, 2002
Blacksburg, Virginia

Key Words: Melt Inclusions – MELTS – Thermodynamic
Modeling – Ponza – Spinels – Olivine – Geothermometer – Tahiti.

Copyright 2002, Luca Fedele

STUDIES OF MAGMATIC SYSTEMS

by

Luca Fedele

(ABSTRACT)

Two magmatic systems were investigated using different petrological tools:

1) Origin of Ponza trachyte was studied combining data from MI with trends predicted by thermodynamic modeling. MI data were compared with known phase relations in the ternary feldspar and anorthite-diopside-albite systems to constrain the parameters used in the modeling. MI data are consistent with melt evolution from a basaltic parent via a fractional crystallization mainly of pyroxene and feldspars. These data and the results from the modeling, suggest a genetic link between the Ponza trachyte and coeval alkali olivine basalts on the nearby Ventotene Island.

2) We evaluated the range of magmatic temperatures within the crystallization interval for a basanite with different olivine-spinel geothermometers. While olivine-spinel pair records the evolution of the basanite during crystallization, low temperatures calculated with the geothermometers are unrealistic. This is likely due to the presence of significant amounts of Ti in our magmatic spinels. Indeed Ti is not taken into account in the geothermometers. We tested the possibility of accounting for the presence and effects of Ti using a linear correction for the Fe^{+2} content in our spinels. While this generated more realistic temperatures at the low end of the range, it also increased the dispersion in the data, suggesting that spinel behavior is more complex and that the presence of Ti affects content and site occupancy of other elements as well.

TABLE OF CONTENTS

CHAPTER 1

Melt Inclusion Geochemistry and Computer Modeling of Trachyte Petrogenesis at Ponza, Italy

Geological Settings.....	1
Sample and Melt Inclusions description	4
Analytical techniques	6
<i>Homogenization of Crystallized Melt Inclusions</i>	6
<i>Electron Microprobe Analysis</i>	17
Results	19
Discussion	25
Conclusions	36
References.....	37

CHAPTER 2

Application of the Olivine-Spinel geothermometer to volcanic rocks: An example from Tahitian Basanite.

The Olivine-Spinel Geothermometer	43
Olivine-Spinel data from the Basanite	45
Results	52
Discussion	56
Conclusions	65
References.....	67
VITA	69

List of Figures

Chapter 1

- Fig. 1 – A) Schematic tectonic map of Italy showing the main tectonic blocks. The box outlines the region of the Pontine archipelago shown in the enlargement in (b). ORL = Ortona-Roccamonfina Line. B) Location of Ponza and the Pontine archipelago.....3
- Fig. 2 – Simplified geologic map of Ponza (after Bellucci et al., 1999).5
- Fig. 3 – Melting sequence of a crystallized melt inclusion in plagioclase. At room temperature the inclusion consists of a mass of intergrown, fine-grained, crystals ± glass. By 1092 °C most of the silicates have melted leaving only a mass of fine-grained opaques, which melt between 1092 and 1197 °C. After quenching, the inclusion contains a homogeneous glass and a vapor bubble. Black line is for scale and is 25 μ.7
- Fig. 4 – Compositions of MI and plagioclase host crystals in the system Or-An-Ab. (a) MI define a trend toward the trachyte composition. (b) Tie lines connecting MI compositions with host compositions. Note that increasing Ab content in the host corresponds to MI compositions that are closer to the trachyte composition. Black arrow = melt evolution trend; FH = Furnace Heated, SH = Stage Heated..... 11
- Fig. 5 – Compositions of MI and cpx host crystals in the system An-Di-Ab. The cotectic cpx-plagioclase refers to 1 Atm. pressure (Bowen, 1928); FH = Furnace Heated, SH = Stage Heated. 13
- Fig. 6 – Harker variation diagrams for all melt inclusions analyzed in this study..... 14
- Fig. 7 – Evolution of a basaltic melt composition during fractional crystallization in the system Orthoclase-Albite-Anorthite-H₂O at low pressure. See text for discussion. (modified after Cox et al., 1979)..... 16
- Fig. 8 – Compositions of MI and host crystals (plagioclase, K-feldspar and cpx) plotted in the tetrahedron Or-An-Ab-Di. 18
- Fig. 9 – Comparison of measured compositions of MI and host feldspars with compositions predicted by phase relationships in the system Or-An-Ab at 1Kb (a) and 2 Kb (b). Dashed lines = icophases; solid lines = feldspar solvus labeled in degrees Celsius. Numbers on icophases represent %Ab in plagioclase co-precipitating with K-feldspar. 20
- Fig. 10 – (a) Comparison between the liquid line of descent (LLD) predicted by MELTS (black dots) and the trend indicated by MI data (black arrow). Also shown are host crystal analysis and the cotectic for 1 Kbar. b) Plagioclase, K-feldspar composition and LLD generated by MELTS at 1 Kbar. c) LLD generated by MELTS at 1 Kbar and different f_{O_2} buffer values. d) LLD generated by MELTS at 1 Kbar and different H₂O contents. 24
- Fig. 11 – Compositions of MI plotted vs. solidification index (SI). Solid line = oxide evolution trend predicted by MELTS (starting from VNT3 composition)..... 27

Chapter 2

Fig. 1 – Spinel inclusions in olivine (black arrow). (A) transmitted light; (B) reflected light.	48
Fig. 2a – $Mg/(Mg + Fe^{+2})$ vs $Cr/(Cr + Al)$ plot for spinels inclusions in olivine.	50
Fig. 2b – $Mg/(Mg + Fe^{+2})$ vs $Fe^{+3}/(Cr + Al + Fe^{+3})$ for spinel inclusions in olivine.....	51
Fig. 3 - Temperatures calculated according to Roeder et al. (1979) plotted vs. $Cr/(Cr + Al + Fe^{+3})$ in spinel.	53
Fig. 4 – Temperatures calculated according to Jianping et al. (1995) plotted vs. $Cr/(Cr + Al + Fe^{+3})$	54
Fig. 5 – Temperatures calculated according to Sack and Ghiorso (1991b) plotted vs. $Cr/(Cr + Al + Fe^{+3})$	55
Fig. 6 – Pressure-temperature diagram showing a possible range for formation conditions of the Tahiti basanite: black dot – lower P-T limit based on mantle plume adiabat and dry peridotite solidus; star – upper P-T limit based on dry peridotite solidus and liquidus temperature for the Tahiti basanite (~ 1350 °C, Tracy and Stolper, unpublished data). Mantle Plume adiabat from Class and Goldstein (1997), asthenosphere adiabat from McKenzie and Bickle (1988), Dry Peridotite Solidus from Green (1973) and Old Ocean Basin adiabat from Class and Goldstein, 1997.	57
Fig. 7 – 3-dimensional plot [$\ln K_D$ vs. Y_{Cr}^{sp} vs. $Y_{Fe^{+3}}^{sp}$] for spinel and olivine data (see text for discussion).....	60
Fig. 8 – Relationship between Ti and Cr content in spinels.	61
Fig. 9a – Temperatures calculated according to Roeder et al. (1979) after correction (1) for Ti content (see text for discussion).....	63
Fig. 9b – Temperatures calculated according to Roeder et al. (1979) after the correction (2) for Ti content (see text for discussion).	64

ACKNOWLEDGMENTS

No man is an island it has been said, and in the same way the outcomes of a long period of work and study, as it is that required by a PhD program, cannot be ascribed to a single man. I could not have possibly reached the end of this journey without the help of many..... teachers, family and friends. The list is long but I hope I will not forget anyone. First of all my gratitude goes to my committee members, Robert Bodnar, Benedetto DeVivo, Robert Tracy, Harvey Belkin, Jim Webster and Jim Beard. Their help during these years kept me on track and showed me the light at the end of the tunnel. I am in debt with all the people in the Department of Geological Science at Virginia Tech, their support and friendship went well beyond what a person could expect. A special thought goes to Connie Lowe..... thanks Connie I would have given up without you ☺. To all the graduate students I met during these years, especially my roommates at Sunset (Peter, Mercedes, Jim, Maria, Jeannie), wish you the best of all and please, please, please, come to visit me in Naples!!! Now on the Italian front..... to all my friends who never lost faith in me Come farei senza di voi eh? Ok it is almost over now, thanks to my brother Stefano and last but not least Mamma e Papa'!! Their total support was, is and it will be always AMAZING!!!!

CHAPTER 1

Melt Inclusion Geochemistry and Computer Modeling of Trachyte Petrogenesis at Ponza, Italy.

Melt inclusions (MI) have proven to be a valuable tool to investigate the physico-chemical evolution of magmatic systems, from initial generation in the deep crust or mantle through all of the subsequent processes that operate during ascent and eruption onto the surface (Lowenstern, 1995; Hari et al., 1991; Sobolev, 1996). MI contain samples of melt trapped during crystallization of the magma; hence major and trace element data obtained through MI analysis may be used to constrain and understand petrogenetic processes including fractional crystallization, magma mixing, and contamination (Roedder E., 1979; Lowenstern, 1995; Sobolev, 1996, Frezzotti, 2001). Owing to its location in the Tyrrhenian sea, the island of Ponza, Italy, offers the opportunity to investigate the formation of alkaline magmas generated in a complex geodynamic setting, specifically that of a basin undergoing extension within an overall collisional tectonic framework (Stanley et al., 1985). We present a study of melt inclusions from Ponza, and combine analytical results from melt inclusions with compositional trends predicted by numerical models to investigate the role played by fractional crystallization of a “basaltic magma” in a shallow magma chamber in the origin of the trachytes on Ponza.

Geological Setting

Ponza is the largest of the 5 islands of the Pontine archipelago, a 30 km long chain located in the Gulf of Gaeta. The archipelago can be divided in two groups: Ponza, Palmarola and Zannone on the northwest, and Ventotene and Santo Stefano to the southeast (Fig. 1b). It is located at the intersection of the 41° parallel discontinuity and the Ortona-Roccamonfina line (Fig. 1a). The 41° parallel discontinuity is a dextral transcurrent fault system at the boundary between the northern and southern Tyrrhenian basin (Savelli and Wezel, 1979), while the Ortona-Roccamonfina line (Locardi, 1982) is a late Pliocene dextral strike-slip fault (Patacca et al., 1990) which represents the present-day boundary between the Central and Southern Apennines (Fig. 1a). Ponza is located at the intersection of two

domains that have undergone significantly different styles of tectonic evolution since the late Miocene. Because the rapid opening of the Tyrrhenian basin since late Tortonian times (~ 10-7 Ma) and the development of the arc-shaped thrust belt mountain chain both occurred in a convergent tectonic setting, the evolution of the basin and the Apennine chain poses an interesting tectonic problem. Furthermore, while the northern Tyrrhenian basin underwent moderate extension, the southern experienced significant thinning of the lithosphere and the crust, and reached “close to oceanic characteristics” (Bassi et al., 1997). Various models have been proposed to explain the formation of the Tyrrhenian sea and the Apennine chain. Boccaletti and Guazzone (1972) proposed that the Tyrrhenian sea represents a back-arc marginal basin in a trench-arc-backarc system which migrated from the northwest to reach its current position. In this model the trench is located in the Ionian sea off the coast of Calabria, where the non-volcanic arc is Calabria itself and the Aeolian islands represent the volcanic arc. A concurrent counterclockwise rotation of the Corsica-Sardinia block is responsible for development of the Apennine chain (Fig. 1a). A Benioff zone dipping to the northwest, evidenced by deep earthquake foci, has been suggested by Barberi et al. (1973). Laubscher (1975) and Scandone (1980) inferred the existence of two westward-dipping subduction zones, one located at the eastern margin of the Sardinia-Corsica block and the other at the western margin of the Adria microplate (Adriatic Sea area on Fig. 1a). More recently, Lavecchia and Stoppa (1996) proposed a new model for the tectonic evolution of the region. Based on the characteristics and distribution of volcanism around the Tyrrhenian basin and the discovery of carbonatitic volcanism, they proposed a passive rifting mechanism to explain the origin and evolution of the basin. Turco and Zuppetta (1998) examined the available geological and geophysical data and proposed a kinematic model of the area which is consistent with a passive rifting mechanism.

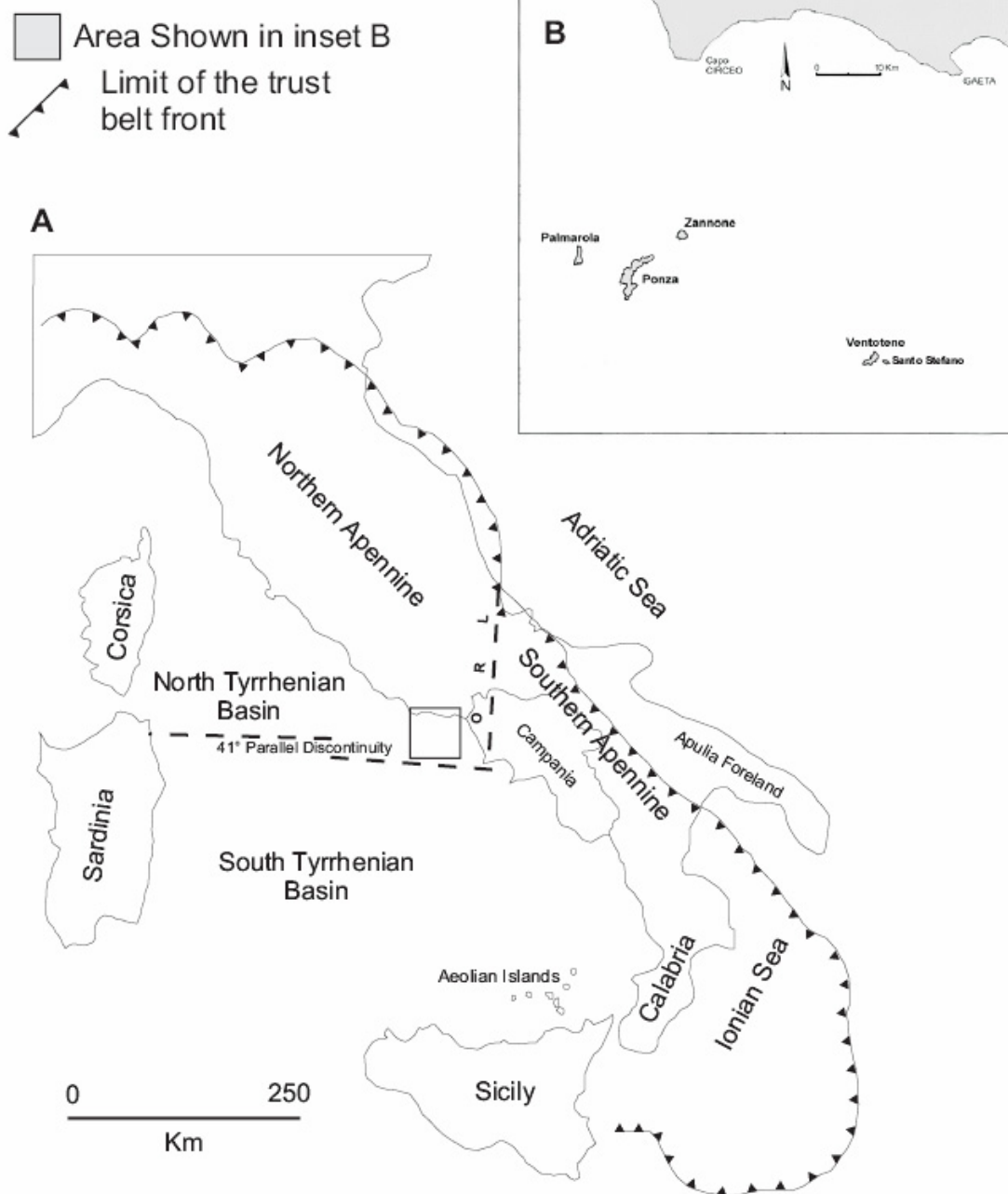


Fig. 1 - A) Schematic tectonic map of Italy showing the main tectonic blocks. The box outlines the region of the Pontine archipelago shown in the enlargement in (b). ORL = Ortona-Roccamonfina Line. B) Location of Ponza and the Pontine archipelago

Ponza is composed of two volcanic units, an older silica-rich (Pliocene) unit that occurs in the northern and central part of the island, and a younger (Pleistocene), alkali-potassic unit that is present only in the southern part of the island (Fig. 2; Bellucci et al., 1999). The older unit, composed of dikes and hyaloclastites of submarine origin, varies in composition from rhyolite to rhyodacite, and in the northernmost part of the island has been affected by an extensive hydrothermal alteration event which caused deep kaolinitization and the formation of bentonite deposits (Pozzuoli, 1988; Ylagan et al., 1996). The younger volcanic products are trachytes, erupted and emplaced above sea level, which form pyroclastic sequences, scoria cones and lava flows. This study focuses on the Ponza trachytes representing the late stages of crystallization of volcanic rocks that are associated with the magmatism in the Campanian area (Conte e Dolfi, 2002; Fig. 1a).

Sample and Melt Inclusions Description.

Samples were collected from all of the volcanic units on Ponza, using the geologic map of Bellucci et al., 1999 to select sampling locations; best-exposed and freshest outcrops occur on the steep cliffs along the coastline. Doubly polished thin sections approximately 200-300 microns thick were made from the collected samples and examined to search for phenocrysts containing melt inclusions suitable for analysis. Only the trachyte samples collected at Punta della Guardia (Fig. 2), which represents the more mafic (primitive) part of the Monte della Guardia trachyte (Conte and Dolfi, 2002), were found to contain useful MI.

The studied rock is porphyritic, with phenocrysts of normally zoned plagioclase (An_{46} to An_{87}), sanidine (Ab_{30} to Ab_{40} , with $An < 10\%$), clinopyroxene (Di_{50} to Di_{69}), and biotite, in order of decreasing abundance. The phenocrysts range in size from 1 to 5 mm and always show abundant fractures.

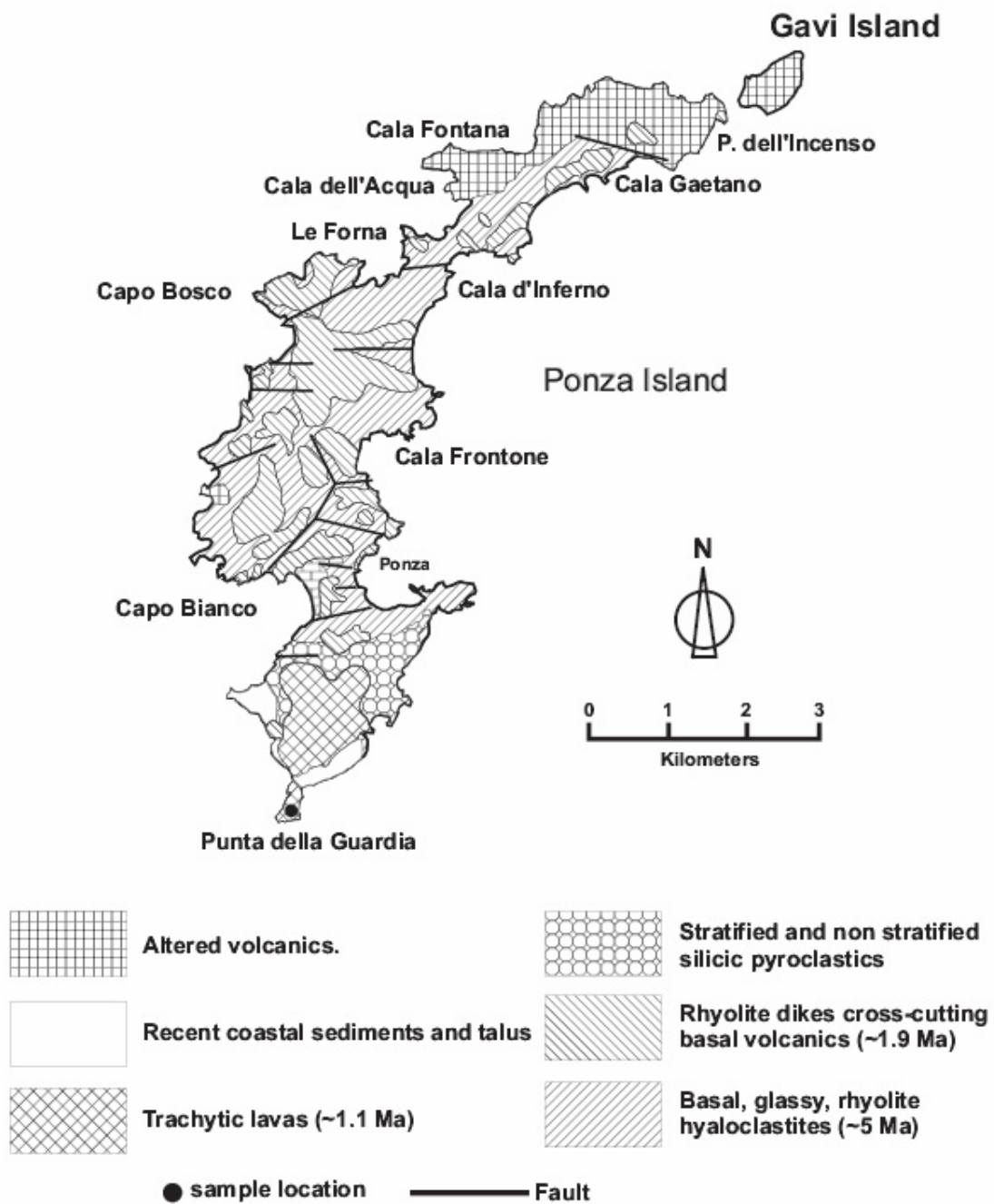


Fig. 2 - Simplified geologic map of Ponza (after Bellucci et al., 1999).

Melt inclusions large enough (> 15 microns) for microthermometric and EMPA analysis were found mainly in plagioclase, and less often in pyroxene and alkali feldspars. The Ponza rhyolites are very fine-grained rocks with only rare, small (typically less than 1 mm) phenocrysts which contained scarce, small (< 10 μm) MI. They proved to be unsuitable for melt inclusion studies.

Melt inclusions (MI) in feldspars and pyroxene range in size from 5 to 50 μm , and their shape is generally spherical or elongated. They are always completely crystallized or devitrified and a bubble is always present, although it is usually not visible until melting begins during heating experiments. MI occur individually or in small clusters, and not along fractures, and can be considered primary. Commonly, they contain small opaque crystals which melt during the heating runs.

A first attempt to extract phenocrysts from the trachyte by crushing proved unsuccessful due to the relatively small size of the crystals, which were also easily broken owing to the presence of numerous fractures. Hence, we extracted single crystals containing melt inclusions directly from the thin sections using a hand-held mini drill fitted with diamond bits and using a binocular stereo-microscope.

Analytical Techniques.

Homogenization of Crystallized Melt Inclusions.

With few exceptions, MI in the Ponza trachytes required heating and quenching to obtain an homogeneous glass, as they are partially or totally re-crystallized when found. Indeed, analyzing crystallized MI may generate misleading or useless information about the original melt composition and volatile content if they are not homogenized (Roedder, 1979; Raia et al., 2000). It should be noted, however, that recent advances in laser ablation ICP-MS allow in some cases reliable quantitative analyses of unhomogenized crystallized melt inclusions (Halter et al., 2002).

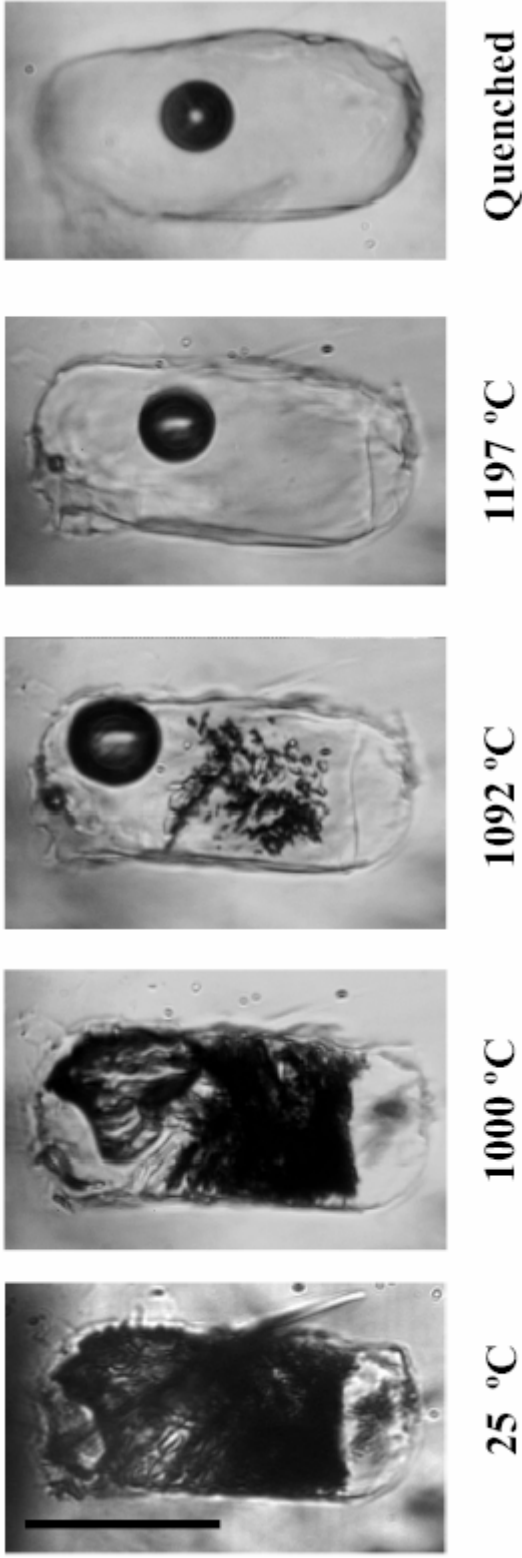


Fig. 3 - Melting sequence of a crystallized melt inclusion in plagioclase. At room temperature the inclusion consists of a mass of intergrown, fine-grained, crystals \pm glass. By 1092 °C most of the silicates have melted leaving only a mass of fine-grained opaques, which melt between 1092 and 1197 °C. After quenching, the inclusion contains a homogeneous glass and a vapor bubble. Black line is for scale and is 25 μ .

Three different approaches are commonly used to re-heat and homogenize crystallized melt inclusions. These include heating melt inclusions contained in doubly-polished wafers, using a one-atmosphere stage mounted on a petrographic microscope (Sobolev, 1996), using a one-atmosphere furnace (Sinton et al., 1993; Nielsen et al., 1995), or heating the inclusions under high confining pressure in a cold-seal autoclave (Student and Bodnar, 1999; Thomas et al., 2000). Each of these techniques offers advantages and disadvantages, depending on the nature of the samples and the type of information sought (Lowenstern, 1994; Nielsen et al., 1998; Student and Bodnar, 1999; Yang and Bodnar, 1994).

Nielsen et al. (1998) report that a major disadvantage of the microscope heating stage technique is that extensive sample preparation is required, and that production of doubly polished sections can introduce microfractures that allow loss of volatiles or other components from the inclusions during heating. However, studies of fluid inclusions in soft and/or easily cleavable minerals such as calcite, fluorite and barite by various workers over the past few decades has led to the development of mineral-friendly sample preparation techniques to significantly minimize the introduction of microfractures during sample preparation (Bodnar and Bethke, 1984; Ulrich and Bodnar, 1988).

The presence of volatiles (e.g. H₂O) can also affect the behavior of melt inclusions during homogenization experiments if the volatiles diffuse out of the MI during heating (Roedder, 1984). This may produce melt inclusions with compositions different from that of the melt originally trapped. Sobolev et al. (1980) reported that slow heating rates can favor loss of volatiles through hydrogen diffusion.

	K-feldspar MI										Plagioclase MI - Heated with Linkam and Vemadsky stages									
	(1) - A	(1) - B	(1) - C	(1) - A	(1) - B	(2) - C	(2) - D	(1) - E	(1) - F	(1) - G	(2) - H	(1) - I	(1) - L	(1) - M	(1) - N	(2) - O	(1) - P	(1) - Q		
SiO2	59.67	59.94	55.92	57.30	57.91	59.14	60.07	61.78	60.68	59.38	58.15	58.18	57.39	57.60	56.29	57.89	57.69	57.61		
TiO2	0.02	0.03	0.08	0.71	0.64	0.82	0.89	0.65	0.67	0.56	0.39	0.55	0.45	0.68	0.43	0.36	0.36	0.37		
Al2O3	18.61	18.40	17.93	20.30	20.18	20.30	19.05	19.11	19.32	21.62	21.95	20.89	21.68	21.14	20.03	21.51	22.25	22.61		
MgO	1.04	0.96	1.43	0.72	0.75	0.75	0.62	0.57	0.65	0.44	0.44	0.48	0.65	0.65	0.70	0.41	0.35	0.33		
CaO	6.98	6.83	9.56	3.44	2.96	3.43	2.76	2.39	2.70	3.64	3.50	3.39	3.64	3.17	3.30	3.51	4.36	4.49		
MnO	0.33	0.32	0.89	0.05	0.10	0.13	0.11	0.12	0.15	0.06	0.10	0.16	0.09	0.06	0.14	0.12	0.06	0.14		
FeO	2.36	2.35	2.40	4.08	3.83	4.15	3.68	3.31	3.40	2.94	2.58	2.75	2.51	3.58	4.01	2.51	2.45	2.48		
Na2O	4.26	4.25	4.10	4.57	5.18	3.13	4.29	3.27	3.60	4.07	5.27	4.61	5.00	4.97	5.31	5.71	5.72	5.60		
K2O	7.14	7.29	5.85	6.21	6.26	6.18	5.83	5.63	5.60	6.53	6.29	6.45	6.24	5.77	6.11	5.48	5.10	5.20		
P2O5	0.02	0.05	0.15	0.27	0.29	0.29	0.83	0.77	0.79	0.27	0.16	0.22	0.12	0.28	0.24	0.20	0.14	0.21		
F	0.41	0.00	0.00	0.14	0.15	0.24	0.21	0.21	0.24	0.18	0.34	0.20	0.06	0.16	0.20	0.20	0.12	0.11		
Cl	0.00	0.01	0.03	0.18	0.15	0.17	0.02	0.01	0.01	0.23	0.23	0.20	0.14	0.16	0.18	0.15	0.16	0.12		
TOTAL	100.83	100.42	98.33	98.06	98.40	98.76	97.78	97.81	97.82	99.92	99.48	98.08	97.76	98.22	97.23	98.11	98.77	98.27		

	Plagioclase MI - Heated with Linkam and Vemadsky stages										Plagioclase MI - heated in one atmosphere furnace									
	(1) - R	(1) - S	(1) - T	(1) - U	(1) - V	(1) - W	(1) - X	(1) - Y	(1) - Z	(1) - AA	(1) - AB	(2) - AC	(1) - AD	(1) - AE	(2) - AF	(1) - AG	(1) - AH	(1) - AI		
SiO2	59.92	58.42	60.36	54.96	52.40	54.91	53.51	55.44	52.63	48.86	49.19	49.00	48.54	47.66	48.47	50.94	49.45	49.45		
TiO2	0.44	0.42	0.43	1.20	0.96	0.39	0.57	0.17	0.72	1.73	1.64	1.65	1.82	1.83	1.86	1.48	1.35	1.35		
Al2O3	19.75	21.32	20.16	18.87	21.92	22.07	23.91	22.99	21.68	18.93	19.12	19.78	20.15	19.59	20.22	20.71	21.75	21.75		
MgO	0.58	0.57	0.60	1.17	1.23	0.73	0.35	0.58	0.83	3.72	3.76	3.87	2.99	3.40	3.14	2.68	1.89	1.89		
CaO	3.36	4.04	4.14	3.48	6.96	5.60	8.09	6.73	5.88	7.89	7.75	7.89	7.30	6.32	6.80	6.58	7.42	7.42		
MnO	0.14	0.18	0.22	0.16	0.06	0.12	0.22	0.08	0.17	0.20	0.20	0.15	0.19	0.18	0.20	0.16	0.14	0.14		
FeO	3.06	2.85	2.30	4.94	4.19	4.18	2.09	2.76	4.26	8.05	8.33	8.14	7.34	8.31	7.70	6.60	6.06	6.06		
Na2O	5.42	5.52	5.59	5.85	5.06	4.78	6.54	5.37	4.72	4.72	4.67	4.84	5.21	5.64	5.52	5.62	6.50	6.50		
K2O	5.83	5.39	6.01	4.92	3.98	3.27	2.92	3.68	4.62	3.51	3.41	3.36	4.27	4.37	4.52	4.53	4.25	4.25		
P2O5	0.17	0.15	0.13	0.53	0.08	0.26	0.22	0.25	0.20	0.73	0.70	0.85	0.63	0.65	0.69	0.47	0.50	0.47		
F	0.36	0.25	0.22	0.53	0.00	0.00	0.71	0.00	0.20	0.25	0.20	0.23	0.23	0.68	0.59	0.50	0.47	0.47		
Cl	0.13	0.16	0.02	0.00	0.00	0.01	0.15	0.16	0.23	0.16	0.17	0.16	0.18	0.20	0.19	0.17	0.13	0.13		
TOTAL	99.15	99.27	100.17	96.63	96.84	96.32	99.26	98.20	97.11	98.74	99.22	99.92	99.16	98.82	99.65	100.43	99.91	99.91		

	CPX MI - Heated with Linkam and Vemadsky stages										
	(1) - A*	(1) - B*	(1) - C*	(1) - D*	(1) - E*	(1) - F*	(1) - G*	(1) - H*	(1) - I*	(1) - M*	
SiO2	46.49	56.47	50.86	57.77	39.62	44.40	54.79	50.28	51.26	52.42	51.23
TiO2	0.56	0.52	0.99	0.90	0.64	4.02	0.32	0.60	0.30	0.58	0.49
Al2O3	9.83	13.92	12.33	16.04	7.59	10.74	11.23	10.29	11.47	10.97	12.56
MgO	5.64	2.42	4.06	3.29	5.69	4.41	4.93	5.74	6.08	5.75	4.20
CaO	14.81	7.84	17.48	6.52	18.28	10.81	10.46	11.53	10.41	10.43	10.78
MnO	0.39	0.29	0.05	0.38	0.31	0.69	0.45	0.45	0.23	0.52	0.22
FeO	11.20	5.45	4.39	4.51	14.37	15.47	5.24	10.29	11.40	11.67	9.37
Na2O	2.52	4.77	3.15	3.62	1.25	2.90	3.16	3.11	3.23	3.15	3.34
K2O	1.27	3.94	2.15	3.91	0.75	3.16	3.89	2.44	2.63	2.56	2.91
P2O5	2.73	1.02	2.40	0.28	6.03	0.62	0.83	1.96	0.58	0.21	1.00
F	0.00	0.41	0.00	0.27	1.28	0.00	0.00	0.00	0.00	0.24	0.00
Cl	0.00	0.00	0.05	0.04	0.00	0.03	0.09	0.00	0.03	0.04	0.00
TOTAL	95.44	97.03	97.91	97.53	95.79	97.26	95.38	96.70	97.62	98.54	96.10

	CPX MI - Heated in one atmosphere furnace									
	(1) - A*	(1) - B*	(1) - C*	(1) - D*	(1) - E*	(1) - F*	(1) - G*	(1) - H*	(1) - I*	(1) - L
SiO2	40.71	40.50	44.72	44.57	47.49	47.79	46.62	44.79	43.54	43.54
TiO2	0.91	0.95	0.44	0.56	1.74	2.12	2.03	2.41	2.77	2.77
Al2O3	6.36	6.99	10.06	10.23	15.39	14.54	14.43	13.08	13.21	13.21
MgO	5.91	5.87	5.94	6.00	6.87	7.06	7.05	9.70	9.54	9.54
CaO	19.50	19.50	18.46	18.71	11.91	12.01	12.02	12.17	10.30	10.30
MnO	0.51	0.58	0.48	0.53	0.06	0.04	0.05	0.06	0.15	0.15
FeO	15.33	15.79	9.91	10.02	7.76	7.91	7.97	9.27	11.12	11.12
Na2O	1.85	1.75	2.45	2.46	2.18	2.16	2.13	2.28	2.86	2.86
K2O	0.55	0.56	0.99	1.01	3.25	3.12	2.96	2.15	2.35	2.35
P2O5	6.17	6.38	5.48	5.38	0.37	0.44	0.51	0.34	0.52	0.52
F	0.05	0.04	0.06	0.06	0.18	0.20	0.20	0.21	0.38	0.38
Cl	0.01	0.01	0.02	0.02	0.08	0.08	0.09	0.07	0.09	0.09
TOTAL	97.85	98.92	99.00	99.53	97.26	97.46	96.04	96.53	96.81	96.81

Tab. 1a - MI compositions. In parenthesis are number of repeated analyses on a single MI (average shown). Letters refer to corresponding host analysis (Tab. 1b). Compositions of MI in CPX denoted with an asterisk are contaminated with apatite (corrected compositions are reported in Table 5).

Tab. 1b - Host crystal compositions. PF10 is Ponza trachyte.

	K-feldspar Host										Plagioclase Host (Stage)									
	A	B	C	A	B	C	D	E	F	G	H	I	L	M	N	O				
SiO2	64.54	63.36	63.78	55.83	55.78	54.84	56.26	56.37	56.60	56.34	55.32	55.32	54.70	55.62	55.55	55.55				
TiO2	0.05	0.05	0.03	0.09	0.02	0.07	0.04	0.10	0.14	0.10	0.10	0.05	0.02	0.02	0.11	0.01				
Al2O3	19.64	19.65	19.58	26.64	27.42	28.04	26.94	26.75	27.11	27.35	27.67	27.67	27.66	28.29	28.35	27.77				
MgO	0.01	0.03	0.02	0.04	0.01	0.03	0.05	0.04	0.03	0.05	0.03	0.03	0.02	0.04	0.02	0.05				
CaO	0.69	0.82	1.13	11.13	10.29	10.82	9.28	9.54	9.55	10.12	10.53	10.53	10.88	10.85	10.42	10.15				
MnO	0.00	0.01	0.03	0.04	0.03	0.05	0.02	0.11	0.09	0.03	0.04	0.04	0.02	0.03	0.05	0.02				
FeO	0.12	0.20	0.33	0.53	0.47	0.31	0.38	0.42	0.48	0.45	0.52	0.52	0.54	0.61	0.51	0.62				
Na2O	3.25	3.18	3.74	4.67	5.04	4.67	5.36	5.33	5.33	5.00	5.01	5.01	4.55	4.86	5.19	5.10				
K2O	9.83	9.45	9.15	0.70	0.85	0.76	1.09	0.97	0.94	0.95	0.79	0.79	0.65	0.61	0.77	0.83				
P2O5	0.02	0.02	0.03	0.03	0.06	0.07	0.03	0.07	0.05	0.10	0.06	0.06	0.07	0.02	0.02	0.02				
F	0.00	1.34	0.07	0.16	0.22	0.11	0.27	0.05	0.23	0.02	0.08	0.08	0.19	0.05	0.11	0.18				
Cl	0.02	0.00	0.02	0.01	0.02	0.01	0.04	0.00	0.01	0.01	0.00	0.00	0.02	0.03	0.02	0.02				
TOTAL	98.17	98.20	97.88	101.87	100.21	99.79	99.76	99.73	100.56	100.52	100.10	100.10	99.31	101.05	101.11	100.33				

	Plagioclase Host (Stage)										Plagioclase Host (Furnace)									
	P	Q	R	S	T	U	V	W	X	Y	Z	AA	AB	AD	AE	AH				
SiO2	56.31	55.23	56.75	56.44	56.38	50.84	50.62	51.47	47.65	47.56	46.92	46.71	46.62	45.64	46.06	47.69				
TiO2	0.05	0.07	0.06	0.09	0.04	0.00	0.00	0.12	0.00	0.02	0.20	0.01	0.00	0.00	0.01	0.01				
Al2O3	27.62	28.28	27.70	27.96	27.47	30.36	30.38	29.64	31.95	32.70	32.30	33.82	33.91	34.24	34.10	32.81				
MgO	0.03	0.03	0.04	0.07	0.02	0.05	0.07	0.05	0.13	0.00	0.00	0.10	0.07	0.03	0.04	0.05				
CaO	9.89	10.67	9.64	9.76	9.73	13.31	13.03	12.85	15.76	16.59	16.07	16.98	17.20	17.83	17.83	16.15				
MnO	0.01	0.07	0.03	0.02	0.07	0.05	0.17	0.26	0.09	0.01	0.11	0.00	0.00	0.00	0.00	0.00				
FeO	0.45	0.33	0.32	0.48	0.55	0.58	0.21	0.61	1.98	0.41	0.87	0.59	0.52	0.53	0.56	0.54				
Na2O	5.36	4.88	5.16	5.25	4.40	3.11	3.41	2.90	2.07	1.74	2.05	1.56	1.30	1.13	1.41	2.04				
K2O	0.75	0.70	1.02	0.92	0.92	0.21	0.36	0.39	0.08	0.11	0.17	0.11	0.10	0.09	0.09	0.21				
P2O5	0.00	0.02	0.04	0.00	0.04	0.00	0.06	0.00	0.00	0.12	0.00	0.03	0.03	0.02	0.04	0.01				
F	0.22	0.00	0.10	0.19	0.16	0.00	0.00	0.21	0.00	0.00	0.00	0.00	0.00	0.00	0.00	0.00				
Cl	0.01	0.03	0.00	0.03	0.03	0.07	0.00	0.00	0.00	0.04	0.00	0.00	0.01	0.00	0.00	0.01				
TOTAL	100.72	100.30	100.87	101.20	99.81	98.68	98.30	98.50	99.71	99.29	98.70	99.92	99.76	99.51	100.14	99.52				

	CPX Host (Stage)										CPX Host (Furnace)									
	A	B	C	D	E	F	H	I	A	B	D	E	I	PF10						
SiO2	48.65	52.22	48.89	50.50	48.23	50.35	50.44	52.32	51.90	50.70	51.69	48.02	48.758	58.41						
TiO2	1.50	0.39	1.13	0.97	1.40	0.82	0.76	0.39	0.55	0.85	0.50	1.91	1.719	0.78						
Al2O3	5.22	1.75	4.19	3.87	4.34	3.20	2.39	1.90	2.42	3.84	3.51	5.90	5.423	18.74						
MgO	13.26	11.51	11.65	13.47	12.88	12.13	12.41	12.54	13.49	12.85	12.84	13.39	13.615	1.42						
CaO	21.37	21.40	21.33	21.21	21.34	21.30	21.97	21.34	22.01	22.14	21.99	21.87	21.913	4.17						
MnO	0.27	0.61	0.60	0.40	0.20	0.49	0.47	0.61	0.31	0.37	0.47	0.17	0.164	0.12						
FeO	7.71	10.17	9.22	8.14	8.18	8.03	9.39	9.97	8.93	9.07	9.53	7.61	7.528	4.67						
Na2O	0.55	0.49	0.31	0.48	0.45	0.62	0.73	0.55	0.45	0.53	0.52	0.41	0.402	6.64						
K2O	0.03	0.04	0.00	0.02	0.10	0.00	0.00	0.00	0.00	0.00	0.01	0.00	0.000	4.87						
P2O5	0.00	0.00	0.00	0.05	0.24	0.09	0.18	0.00	0.01	0.02	0.02	0.02	0.026	0.30						
F	0.52	0.50	0.15	0.00	0.19	0.39	0.00	0.00	0.00	0.00	0.00	0.00	0.000	NA						
Cl	0.00	0.00	0.03	0.00	0.00	0.00	0.06	0.02	0.00	0.01	0.00	0.00	0.006	NA						
TOTAL	99.09	99.09	97.48	99.11	97.35	97.21	99.18	99.64	100.07	100.39	101.07	99.29	99.554	100.12						

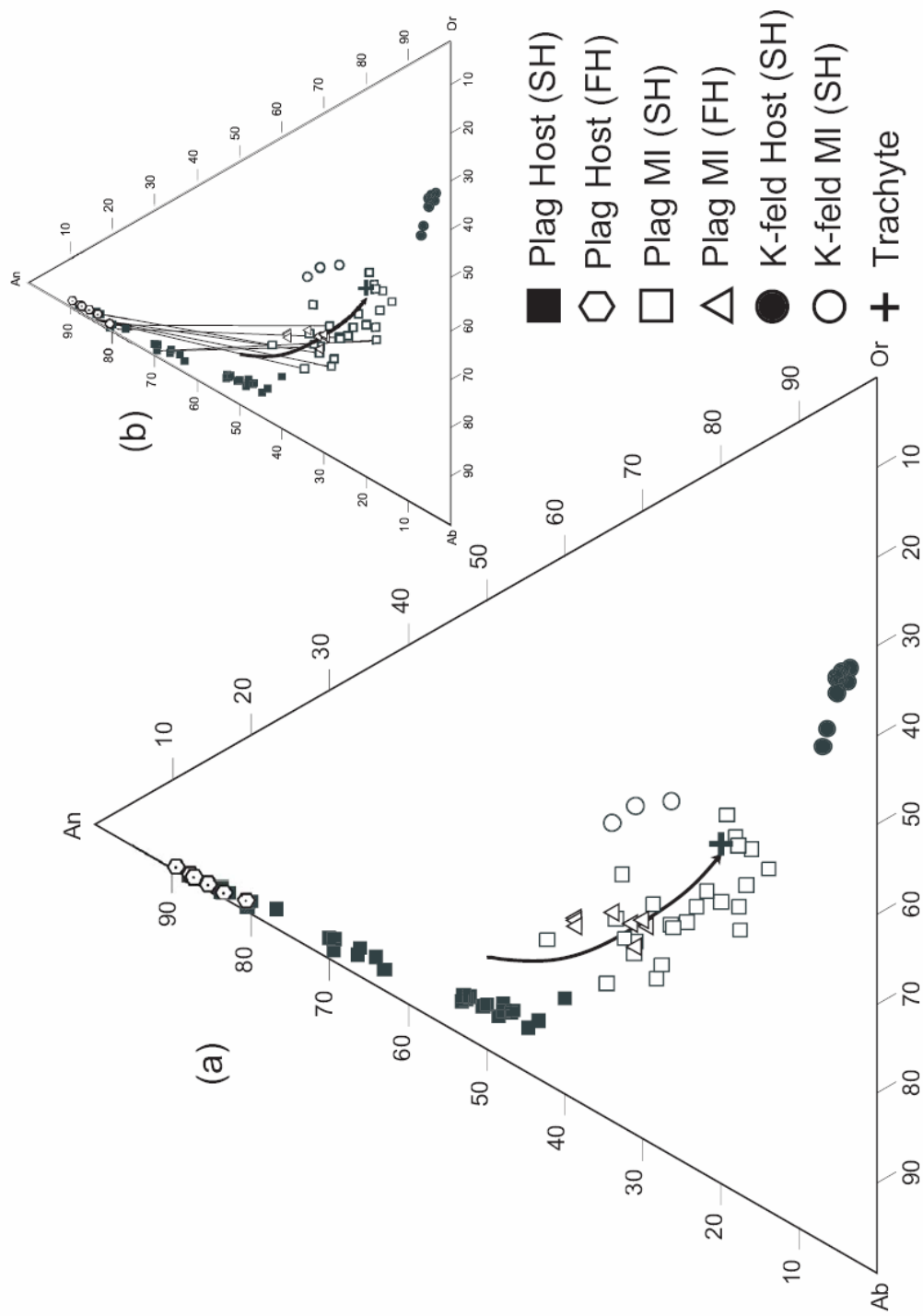


Fig. 4 - Compositions of MI and plagioclase host crystals in the system Or-An-Ab. (a) MI define a trend toward the trachyte composition. (b) Tie lines connecting MI compositions with host compositions. Note that increasing Ab content in the host corresponds to MI compositions that are closer to the trachyte composition. Black arrow = melt evolution trend; FH = Furnace Heated, SH = Stage Heated.

This, in turn, results in an increase in the final homogenization temperature, a different melting behavior and, most importantly, modified (incorrect) compositions of the MI. In this case the duration of the heating event can be critical, and analysis of heated and un-heated MI can help to place constraints on the extent of volatile loss during heating (Raia et al., 2000).

One of the main advantages of studying melt inclusions in doubly polished wafers is that inclusions can be observed not only before and after, but also during heating (Danyushevsky et al., 2002). Also, melt inclusions may trap solid phases along with the melt, and if these solids are incorporated back into the melt during heating, a wide range in melt compositions would result, with the variability being a function of the relative size of the trapped solid phases. If the inclusions are not observed before and during heating, the heterogeneous nature of the inclusions would not be recognized and the resultant range in MI compositions might be incorrectly interpreted to be the result of petrogenetic processes. For example, in the present study, evidence suggests that apatite was trapped along with melt in some inclusions in clinopyroxene, as described below.

In order to observe the melting behavior of the inclusions, we used microscope-mounted heating stages with slow heating rates. During the experiments no decrepitation phenomena were observed, hence it was not necessary to heat the inclusions under pressure. To confirm that the slow heating rates did not affect the compositions and the melting behavior of the inclusions as reported by Sobolev et al. (1980; i.e. loss of H₂O), some short-duration heating experiments were conducted in a one atmosphere furnace, and the results compared to the longer duration experiments. However, even short duration heating does not completely rule out the possibility that some water may be lost by diffusion during the experiments (Skirius et al., 1990; Qin et al., 1992; Lowenstern, 1994).

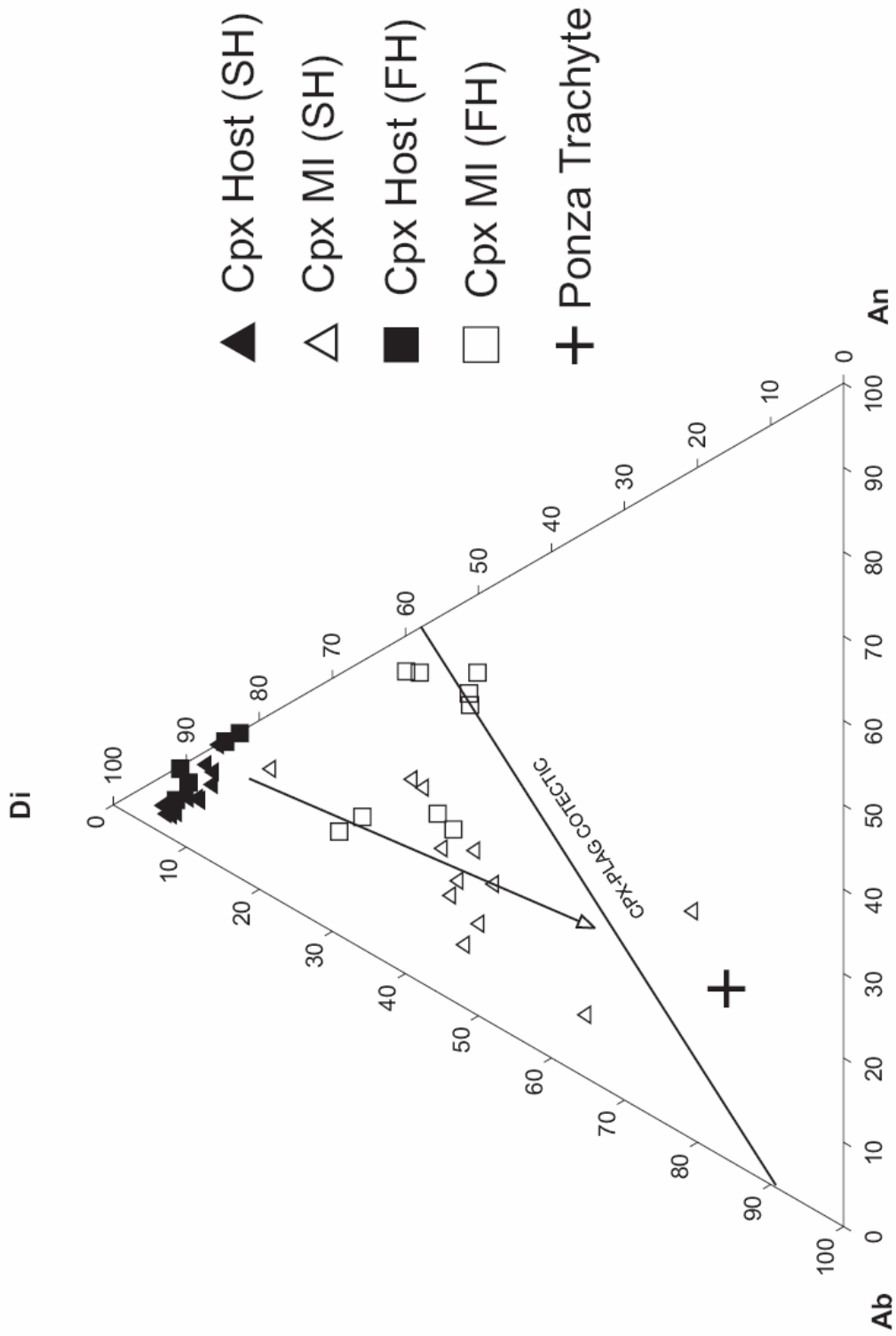


Fig. 5 - Compositions of MI and cpx host crystals in the system An-Di-Ab. The cotectic cpx-plagioclase refers to 1 Atm. pressure (Bowen, 1928); FH = Furnace Heated, SH = Stage Heated.

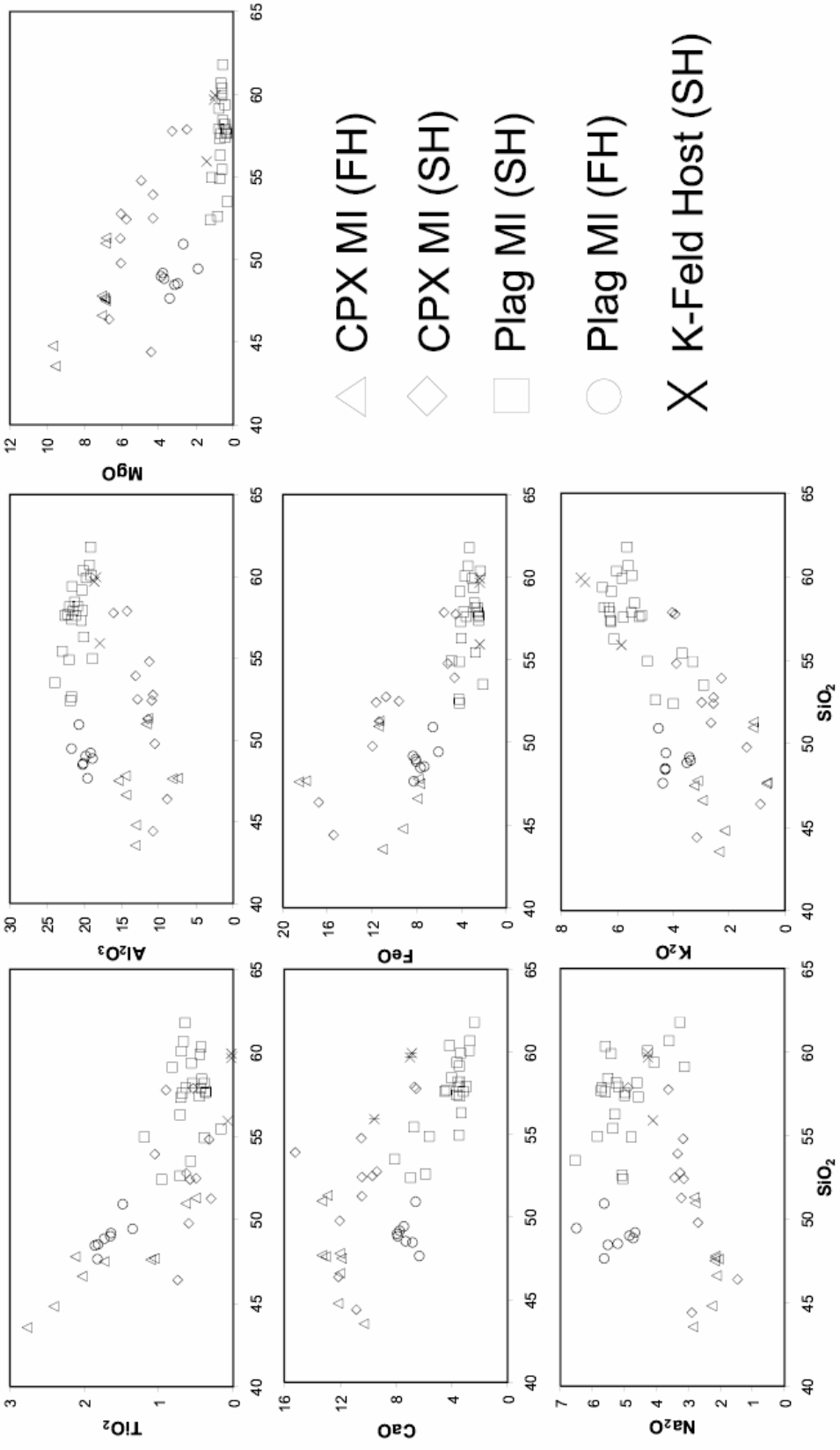


Fig. 6 – Harker variation diagrams for all melt inclusions analyzed in this study.

Melt inclusions were heated in either a high temperature (1500°C) Linkam stage, or a Vernadsky heating stage (Sobolev et al., 1980), or a one atmosphere furnace, until complete melting of all crystals was achieved. MI were quenched by removal from the furnace in the Linkam stage, by turning off the power to the Vernadsky stage, or by extraction from the one atmosphere furnace followed by quenching in water. The quenching rates were consequently different. While the Vernadsky stage allows an extremely fast quenching rate (< 1 sec) from high T (1200 °C) to < 800 °C, the Linkam requires at best a few tens of seconds to cool over this same range. The 1 atm furnace allowed quenching from high T to room temperature in less than 3 seconds. We found no differences in temperatures of melting or melting behavior among MI heated in the Linkam stage, the Vernadsky stage or the 1 atm furnace.

All stage experiments were conducted in controlled (inert gas) atmosphere to avoid oxidation of the crystals. Nitrogen was used in the Linkam stage and high-purity helium that was de-oxygenated by passing over hot (600 °C) titanium metal powder was used in the Vernadsky stage. The heating rate for the Linkam stage was computer-controlled using the following heating schedule: 20 °C/min from 0 to 600 °C, 10 °C/min from 600 to 1000 °C, and 5 °C/min from 1000 °C to the final melting temperature. The Vernadsky stage is operated manually using a Variac, so the heating rate cannot be controlled precisely. The temperature was raised slowly over an extended period of time (~ 2 - 3 hours) at an average rate of 5 °C/min. Both stages were calibrated using the melting points of NaCl (801 °C) and Au (1064 °C). The precision and accuracy are ± 5 °C for the Linkam stage and ± 2 °C for the Vernadsky stage at 1000 °C.

In order to test whether the slow heating rates used for the Ponza MI affected the compositions (Sobolev et al., 1980), some inclusions were homogenized using a one

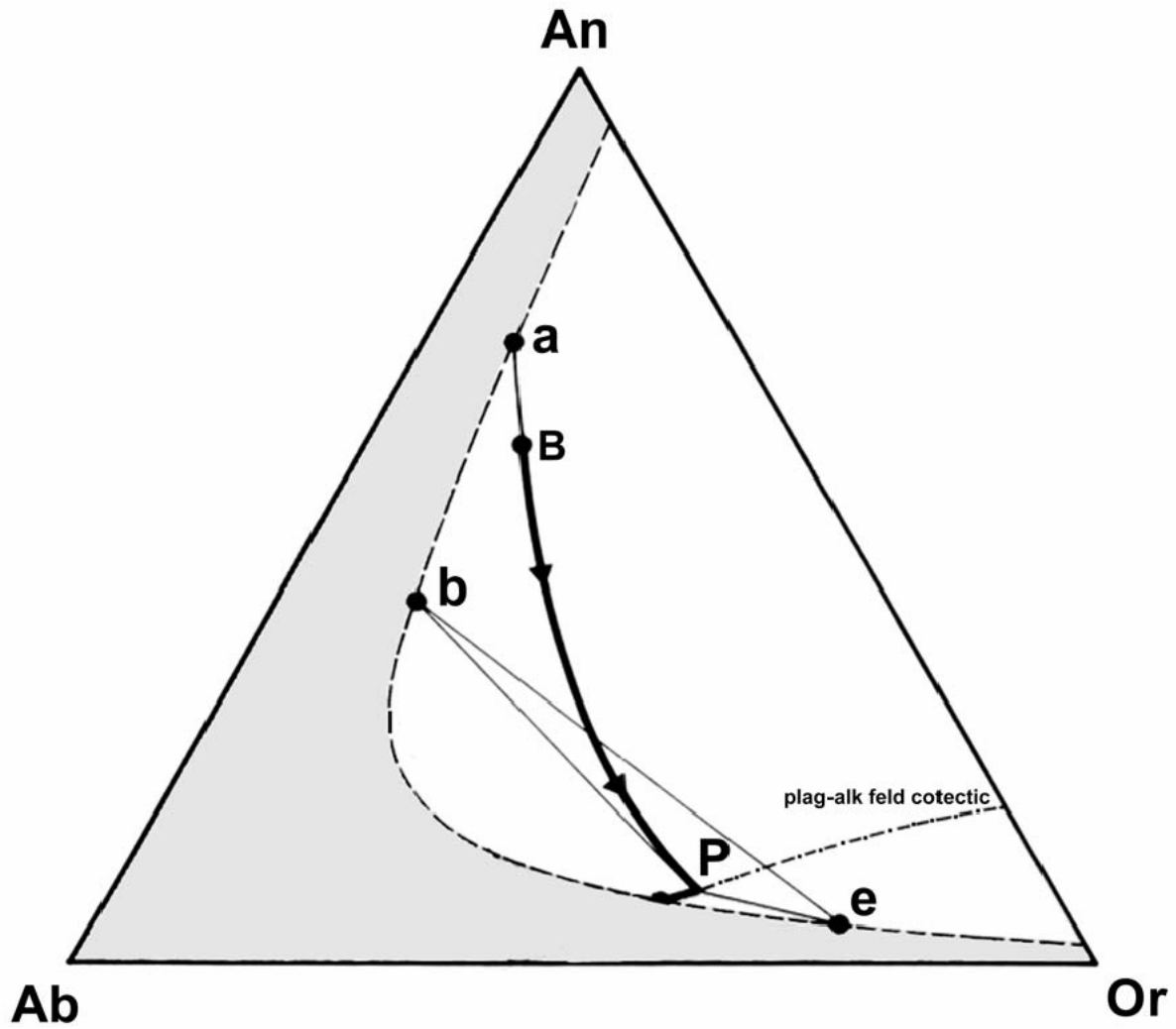


Fig. 7 - Evolution of a basaltic melt composition during fractional crystallization in the system Orthoclase-Albite-Anorthite-H₂O at low pressure. See text for discussion. (modified after Cox et al., 1979).

atmosphere furnace in the Dept. of Earth and Planetary Sciences at the American Museum of Natural History in New York. MI in plagioclase and pyroxene crystals were placed into a platinum capsule, one crystal per run, and introduced into the furnace by sliding the capsule into a quartz tube. The capsule was attached to a ceramic rod to allow for rapid extraction and quenching in water. The furnace was pre-heated to 1170°C, based on step-heating runs carried out at the beginning of the experiments which showed this to be the minimum temperature required to obtain complete melting of the MI. This temperature is in good agreement with the temperatures (1150-1200°C) required for complete melting using the much slower heating rates in the microscope-mounted stages. To avoid oxidation a few drops of immersion oil were placed in the capsule with the crystal according to the technique described by Thomas and Webster (2000). MI were kept at high temperature for 5 minutes and then quenched.

Electron Microprobe Analysis.

Major element analyses for inclusions heated using the Linkam and the Vernadsky stages were performed on a CAMECA SX50 EMPA in the Department of Geological Sciences at Virginia Tech, using a 15 kV and 2 nA defocused (5 µm) beam. The low current was chosen to minimize loss of sodium from the glass through heating by the electron beam. Counting time was 20 s for F and Cl and 10 s for all other elements including Na, which was analyzed as first. The EMPA was calibrated using synthetic and natural minerals of known composition. Inclusions homogenized in the one atmosphere furnace were analyzed at the American Museum of Natural History on a CAMECA SX100 EMPA using a 15 kV defocused beam (5 µm) and a current of 10 nA for all elements except Na, which was analyzed first using a 2 nA beam. Counting times were 80 s for F, 40 s for Cl and Na, 30 s for P and 20 s for all others elements.

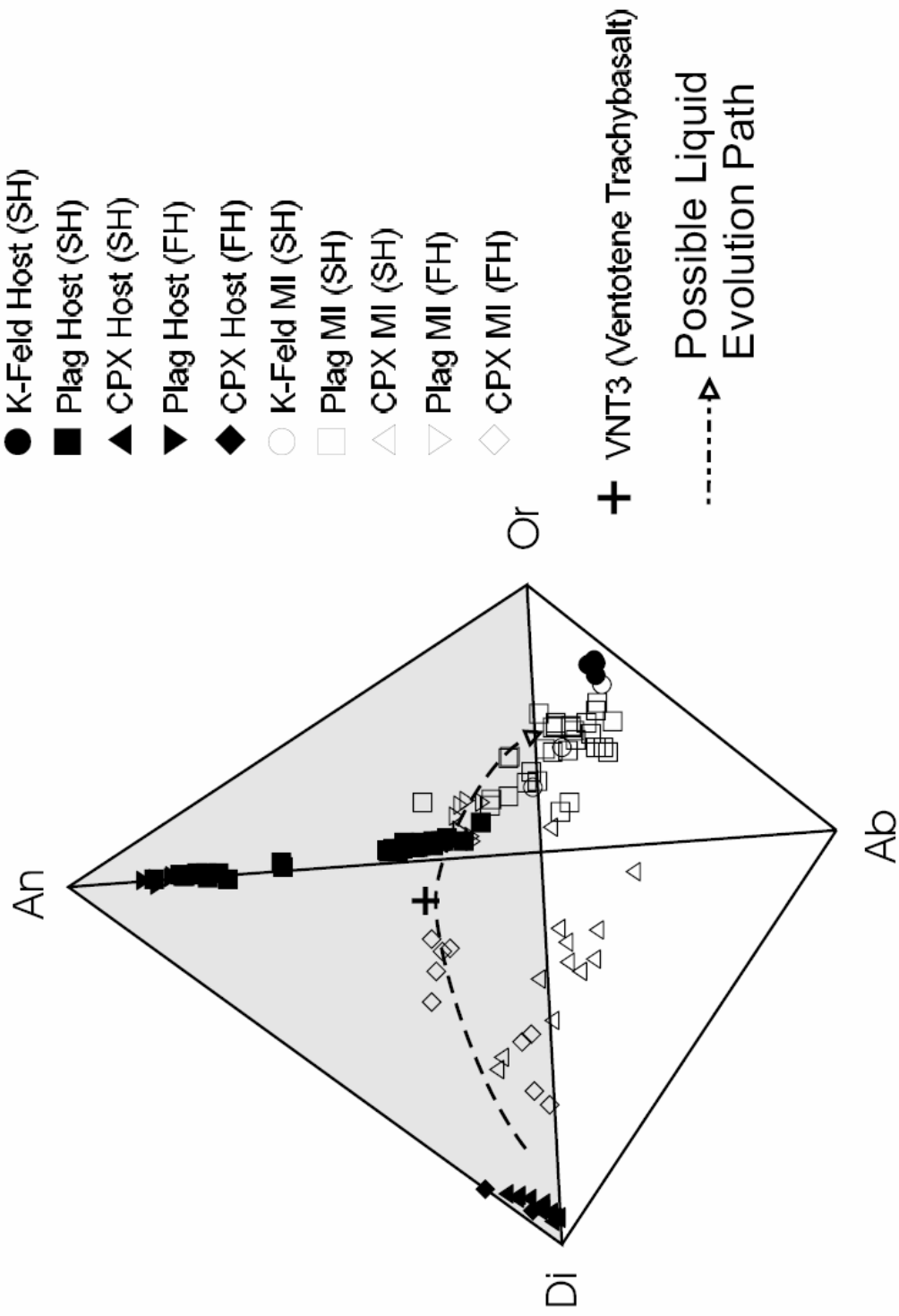


Fig. 8 - Compositions of MI and host crystals (plagioclase, K-feldspar and cpx) plotted in the tetrahedron Or-An-Ab-Di.

The instrument was calibrated using natural minerals of known composition. Only inclusions larger than 15 μ m were used for EMPA analysis to avoid including any of the host phase in the analytical volume for the inclusion. A few larger inclusions were analyzed twice in different spots to test for homogeneity. These repeated analyses confirm that the heating experiments produced homogeneous glasses in the inclusions.

Results.

During heating in the microscope stages, inclusions in plagioclase and K-feldspar showed no detectable melting below 1000 °C, and complete melting of the inclusions occurred between 1150 and 1200 °C. For MI in pyroxene, no melting was detected below 950 °C and complete melting occurred between 1150 and 1200 °C. MI did not noticeably change shape or size during heating, suggesting that relatively little material dissolved from the inclusion walls during the experiments (Fig. 3). However it should be noted that a ten percent increase in volume for an originally 50 micron diameter spherical inclusion would represent less than a one micron increase in inclusion diameter - such a small increase in inclusion size is difficult to detect, either during the heating run or during later petrographic examination.

During early heating runs it was found that if the sample was heated beyond the temperature at which the last crystal melted (in an attempt to homogenize the vapor bubble), the host crystal containing the inclusions showed considerable melting (in some cases it melted completely) causing loss of the MI. We believe that this behavior was triggered by melting of some of the ground mass and/or interstitial glass attached to the crystal. It was not possible to completely remove all ground mass (or interstitial glass) from the phenocrysts after their extraction from the thin sections.

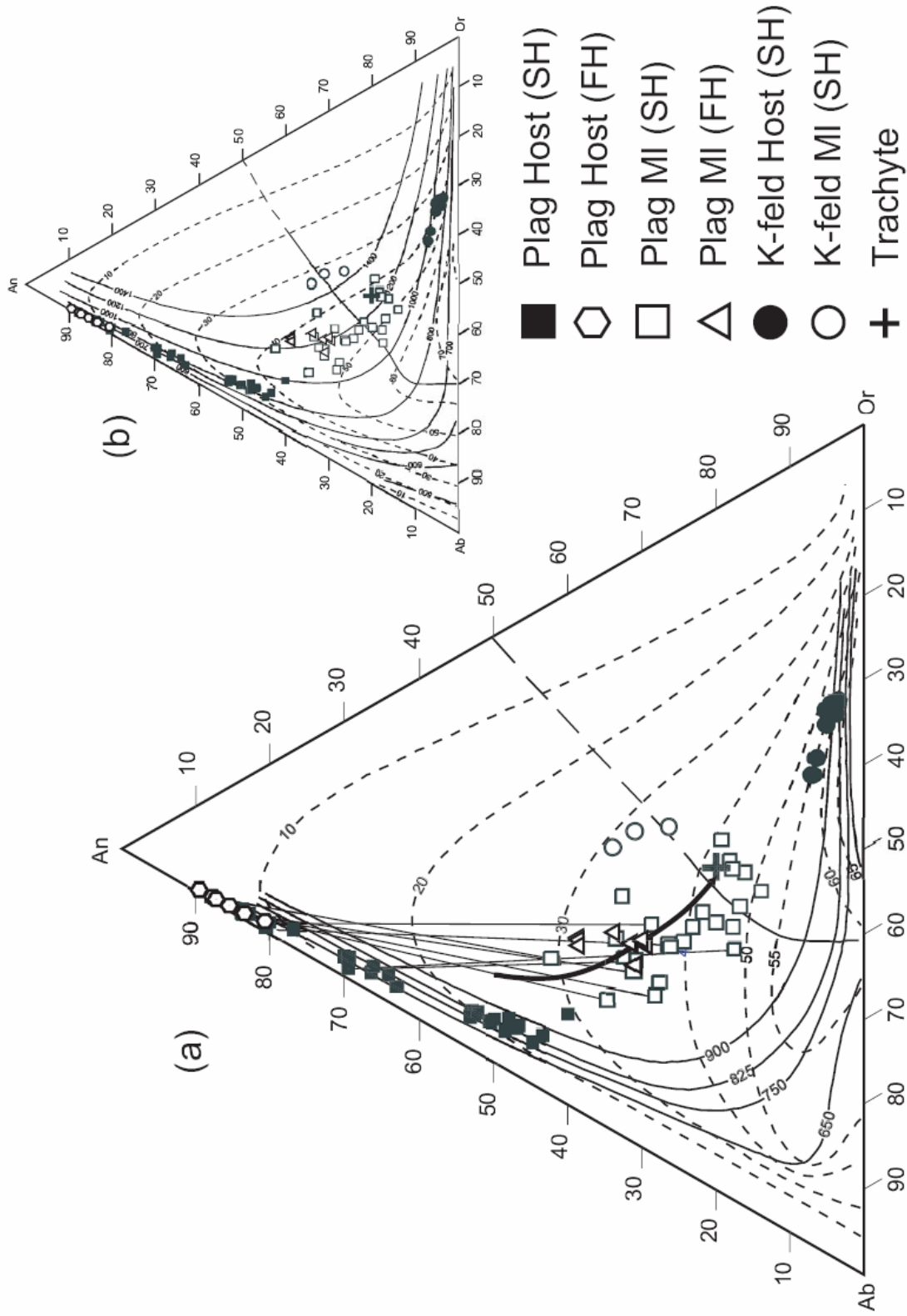


Fig. 9 - Comparison of measured compositions of MI and host feldspars with compositions predicted by phase relationships in the system Or-An-Ab at 1 Kb (a) and 2 Kb (b). Dashed lines = icophases; solid lines = feldspar solvus labeled in degrees Celsius. Numbers on icophases represent %Ab in plagioclase co-precipitating with K-feldspar.

Attempts to do so using dilute acid solutions regularly resulted in loss of the phenocrysts. In order to preserve the MI, it was decided to stop the experiment and quench the samples after the last solid melted. Consequently, complete homogenization of the inclusions (i.e. disappearance of the vapor bubble) was never achieved.

Failure to achieve complete homogenization of the vapor bubble during heating experiments is likely due to the fact that the pressure in the inclusion is less than the confining pressure during entrapment (Student and Bodnar, 1999). Since volatile solubility in the melt is mainly a function of pressure at the moment of trapping, the lower pressure in the inclusion during laboratory experiments requires heating to higher temperature to dissolve the volatiles back into the melt. We do not have an independent estimate of the trapping pressure, although results from the computer modeling suggest that it did not exceed 1 Kb (see discussion). Melting temperatures reported here should not be interpreted as trapping temperatures.

The composition (in wt. % oxides) of MI in plagioclase, K-feldspar and pyroxene is shown in Table 1a, while the composition of the associated phenocryst hosts and the Ponza trachyte is shown in Table 1b. Because MI represent the composition of the melt during its evolution (provided one can rule out post-entrapment modifications of MI composition), it is useful to plot MI data on appropriate phase diagrams (i.e. relevant to the phases present in the rock). This allows one to compare analytical results with experimental data available on phase relationships and liquid evolution paths in the system of interest. However, it should be emphasized that because most experimentally-determined phase diagrams are simplifications of natural systems, perfect agreement between natural MI data and experimentally-determined phase equilibria is unlikely. For this reason, we also plotted our MI data on conventional Harker variation diagrams to allow comparison with other literature data.

Tab. 2 – Variation of liquid composition during cooling as predicted by MELTS. VNT3: Ventotene trachybasalt.

	Start. Comp.	T °C							
		1170	1120	1070	1020	970	920	870	820
VNT3		Liq. Comp.							
SiO ₂	48.83	48.95	49.88	55.7	57.98	57.75	57.3	55.77	52.45
TiO ₂	1.19	1.22	1.67	1.16	1.04	1.03	0.59	0.34	0.12
Al ₂ O ₃	18.54	18.42	18.55	18.7	18.13	18.15	18.03	16.66	14.28
Fe ₂ O ₃	1.5	1.56	1.81	1.11	0.72	0.55	0.55	0.61	0.79
FeO	7.39	7.51	8.66	4.48	2.55	1.81	1.7	1.69	1.76
MnO	0.15	0.15	0.2	0.27	0.36	0.71	1.17	2.38	3.94
MgO	5.76	5.8	3.35	1.67	1.07	0.9	0.72	0.49	0.2
CaO	10.55	10.4	7.47	5.05	4.13	3.73	3.13	2.63	2.27
Na ₂ O	2.32	2.35	3	3.74	4	4.91	6.34	9.06	13.04
K ₂ O	3.02	3.09	4.56	6.82	8.12	7.53	6.19	4.04	2.12
P ₂ O ₅	0.25	0.26	0.38	0.59	0.86	0.91	0.81	0.9	1.2
H ₂ O	0.3	0.31	0.46	0.7	1.04	2.02	3.47	5.42	7.85

Tab. 3 – Phases assemblages on liquidus during cooling as predicted by MELTS

T °C	Phases on the liquidus							% Cryst.
1170	Cpx (Di)	Plag (An)						2.36
1165	Cpx	Plag	Ol (Fo)					7.03
1115	Cpx	Plag	Ol	Sp (Mag)				37.79
1030	Cpx	Plag	Ol	Sp	K-felds			65.82
1025	CPx	Plag		Sp	K-felds			68.83
1000	Cpx	Plag		Sp	K-felds	Ap		78.83
895	Cpx	Plag		Sp	K-felds	Ap	Bi	93.38
875		Plag		Sp	K-felds	Ap	Bi	95.5

Tab. 4 – Comparison of observed and predicted compositions of minerals in the Ponza trachyte.

MINERAL	Composition Range		
		MELTS	Trachyte
Pyroxene	1170-1030 °C	Di [54-43]	Di [69-50]
Plagioclase	1170-875 °C	An [83-32]	An [88-40]
K-feldspar	1030-875 °C	Or [64-63]	Or [66-55]

When plotted on the ternary feldspar phase diagram (Ab-An-Or, Fig. 4) the plagioclase host compositions define a broad range from about An₄₆ to An₈₇ with low but gradually increasing Or content with decreasing An content. K-feldspar host compositions define a more limited range at about Ab₃₀ to Ab₄₀, with An < 10 %. Compositions of MI in plagioclase define a trend that extends from the host compositions toward the composition of the Ponza trachyte. Noticeably, the compositions of the few MI (3) analyzed in K-feldspar plot toward higher An compositions. In the diopside-albite-anorthite ternary (Di-Ab-An, Fig. 5), compositions of MI in pyroxene lie within the diopside field and extend towards the Cpx-Plagioclase cotectic. While MI compositions appear to evolve from the Di apex toward the Cpx-Plagioclase cotectic, a small cluster of MI that were re-heated in the 1 atm furnace plot almost on the cotectic itself. These MI are poorer in Na compared with most other MI in clinopyroxene and might be the result of excess re-melting of the host.

MI data are plotted on Harker variation diagrams vs. SiO₂ (Fig. 6). While all plots show substantial scatter in the MI data, general trends with increasing SiO₂ are easily recognizable. The data show a decrease in TiO₂, MgO, CaO and FeO with increasing SiO₂, and an increase in Al₂O₃, Na₂O and K₂O as SiO₂ increases. At SiO₂ concentrations greater than about 50-55 wt.%, FeO, and to a lesser extent TiO₂ and MgO, become constant. In this same range, the concentrations of Na₂O and Al₂O₃ begin to decrease with increasing SiO₂. CaO and K₂O show a continuous decrease and increase, respectively, with increasing SiO₂. Compositions of MI heated in the microscope stage and MI heated in the 1 atm furnace partially overlap, both for the clinopyroxene and plagioclase groups, as do data for clinopyroxene and plagioclase as a whole.

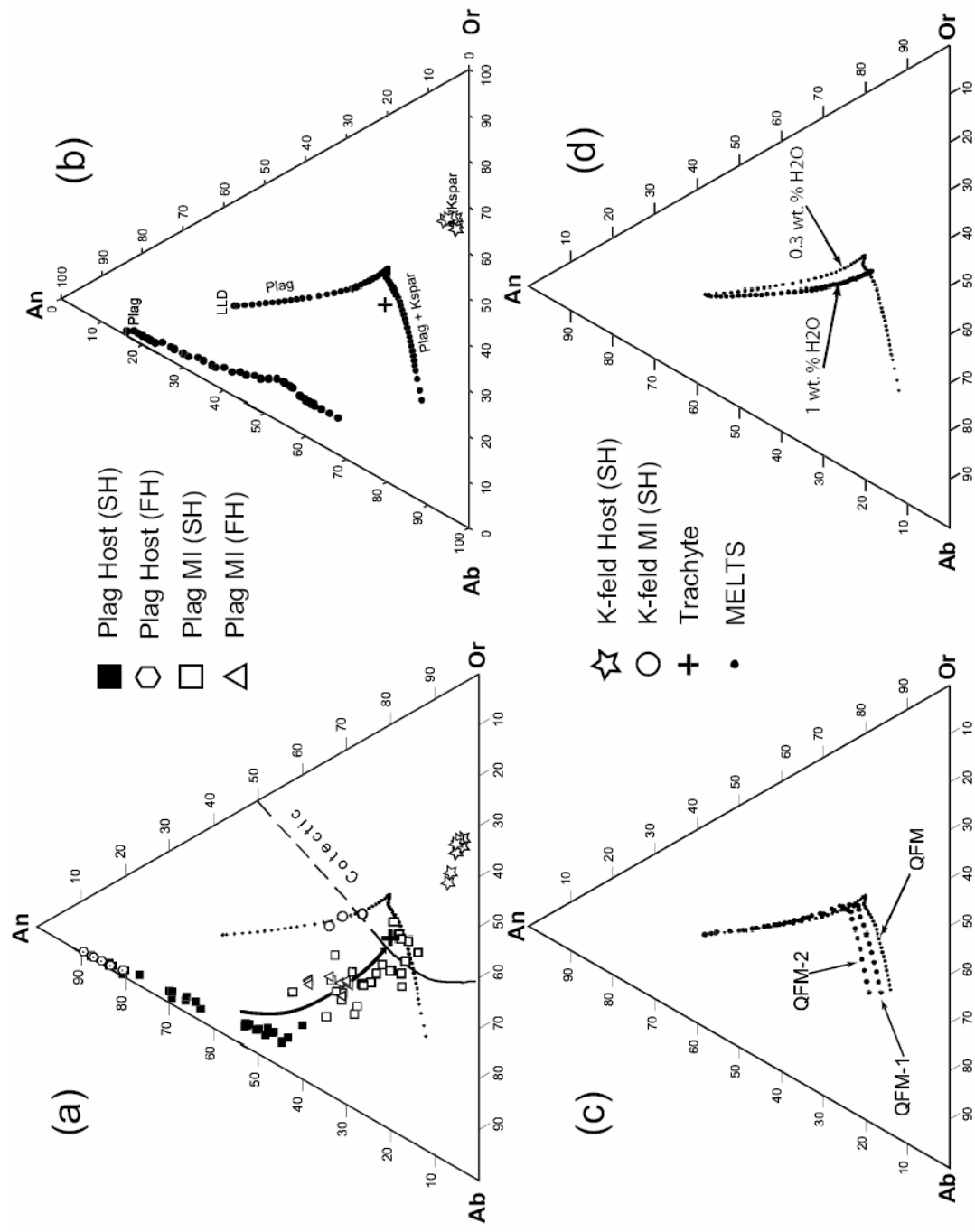


Fig. 10 - (a) Comparison between the liquid line of descent (LLD) predicted by MELTS (black dots) and the trend indicated by MI data (black arrow). Also shown are host crystal analysis and the cotectic for 1 Kbar. b) Plagioclase, K-feldspar composition and LLD generated by MELTS at 1 Kbar. c) LLD generated by MELTS at 1 Kbar and different f_{O_2} buffer values. d) LLD generated by MELTS at 1 Kbar and different H₂O contents.

MI in K-feldspar always plot at the high- SiO_2 end for all elements and overlap with plagioclase MI data. Noticeable is the presence of MI in clinopyroxene with low SiO_2 content and high $\text{CaO}/\text{Na}_2\text{O}$. The composition of these inclusions has been altered by accidentally trapped apatite, as testified by the high P_2O_5 content (Tab. 1a). When recalculated after subtracting the apatite contribution [assuming that all the P represented apatite and using the stoichiometric formula: $\text{Ca}_5(\text{PO}_4)_3\text{OH}$], their compositions result similar to other MI in clinopyroxenes and the $\text{CaO}/\text{Na}_2\text{O}$ ratio decreases (Tab. 5).

Discussion.

A fundamental assumption in every melt inclusion study is that MI are samples of the bulk melt trapped during crystallization of the host crystal. This assumption has been questioned by some workers who suggest that the slow diffusion of components in the melt can induce the formation of boundary layers surrounding growing crystals (Watson et al., 1982; Bacon, 1989). According to this model, incompatible elements are enriched in the boundary layer, whereas compatible elements are depleted. Melts within the boundary layer thus do not represent the composition of the bulk melt and, if trapped in a MI, would provide misleading information on the composition of the melt. This interpretation is supported by recent work by Thomas et al. (2001) which documented the absence of boundary layer effects in melt inclusions trapped in coeval zircon, allanite, quartz and plagioclase from the Toba tuffs.

Based on detailed studies of melt inclusions, it is believed that the effect of chemical gradients within the boundary layer on melt inclusion compositions is negligible for inclusions ≥ 50 μm in diameter (Lu et al., 1995) and is insignificant for inclusions greater than 25 μm (Lowenstern, 1995; Anderson, 1974).

Tab. 5 - MI in CPX corrected for apatite contamination.

MI in CPX after correction for apatite contamination										
	Heated with Linkam and Vernadsky stages						Heated in one atmosphere furnace			
	(1) - A	(1) - B	(1) - C	(1) - E	(1) - H	(1) - M	(1) - A	(1) - B	(1) - C	(1) - D
SiO ₂	49.78	57.87	53.92	46.38	52.76	52.50	47.67	47.61	51.29	50.96
TiO ₂	0.60	0.54	1.05	0.74	0.63	0.50	1.06	1.11	0.50	0.63
Al ₂ O ₃	10.53	14.26	13.07	8.89	10.80	12.87	7.45	8.21	11.54	11.69
MgO	6.04	2.48	4.31	6.66	6.02	4.30	6.92	6.90	6.81	6.86
CaO	12.01	6.67	15.18	12.10	9.39	9.69	13.32	13.05	12.90	13.29
MnO	0.41	0.30	0.05	0.36	0.47	0.23	0.59	0.68	0.55	0.61
FeO	12.00	5.58	4.65	16.82	10.80	9.60	17.96	18.57	11.37	11.45
Na ₂ O	2.70	4.88	3.34	1.46	3.26	3.43	2.16	2.06	2.81	2.80
K ₂ O	1.36	4.03	2.28	0.88	2.56	2.98	0.65	0.66	1.13	1.15
F	n.a.	0.42	n.a.	1.50	n.a.	n.a.	0.06	0.04	0.07	0.07
Cl	n.a.	n.a.	0.05	0.00	n.a.	n.a.	0.02	0.01	0.03	0.02
TOTAL	95.44	97.03	97.91	95.79	96.70	96.10	97.85	98.92	99.00	99.53
CaO/N ₂ O	4.45	1.37	4.54	8.30	2.88	2.83	6.15	6.34	4.59	4.75
SI	27.35	14.62	29.54	25.81	26.60	21.19	24.99	24.49	30.79	30.83

Tab. 6 - MI in Plagioclase corrected for excess remelting of the host.

MI in Plagioclase after subtraction of 25% Host										
	(1) - A	(1) - B	(2) - C	(2) - D	(1) - E	(1) - F	(1) - G	(2) - H	(1) - I	(1) - L
SiO ₂	58.55	58.98	60.78	61.76	64.01	62.63	60.52	59.22	59.54	58.60
TiO ₂	0.92	0.85	1.08	0.92	0.83	0.86	0.72	0.50	0.72	0.60
Al ₂ O ₃	17.88	17.88	17.77	16.54	16.67	16.87	19.75	20.09	18.76	19.80
MgO	0.96	1.00	1.00	0.81	0.75	0.87	0.57	0.58	0.64	0.59
CaO	0.89	0.52	0.97	0.59	0.00	0.42	1.49	1.28	1.02	1.24
MnO	0.05	0.12	0.15	0.14	0.13	0.17	0.08	0.11	0.21	0.12
FeO	5.33	4.98	5.44	4.81	4.30	4.41	3.77	3.27	3.52	3.18
Na ₂ O	4.60	5.26	2.62	3.96	2.60	3.05	3.77	5.36	4.51	5.17
K ₂ O	8.15	8.11	8.02	6.97	7.24	7.23	8.41	8.14	8.39	8.14
P ₂ O ₅	0.36	0.37	0.42	1.10	1.00	1.04	0.32	0.19	0.27	0.13
F	0.14	0.12	0.28	0.19	0.27	0.24	0.23	0.43	0.24	0.01
Cl	0.23	0.20	0.23	0.01	0.01	0.01	0.30	0.30	0.27	0.18
TOTAL	98.06	98.40	98.76	97.78	97.81	97.82	99.92	99.48	98.08	97.76

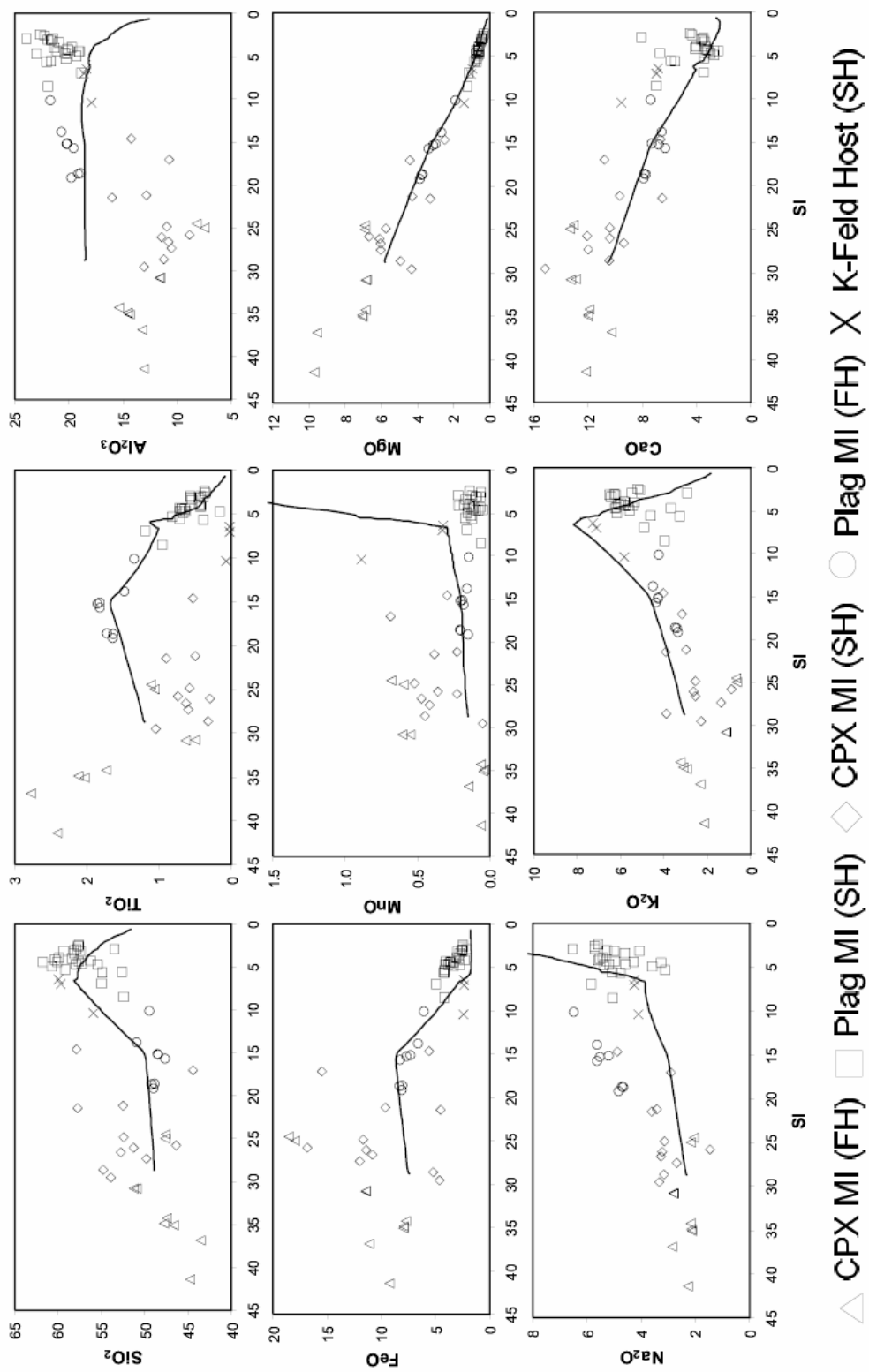


Fig. 11 - Compositions of MI plotted vs. solidification index (SI). Solid line = oxide evolution trend predicted by MELTS (starting from VNT3 composition).

Most of the inclusions used in this study were 25 μm or more in diameter and no correlation between size and composition was observed for the smallest inclusions analyzed. Our interpretation of these observations is that boundary layer processes had little or no effect on melt inclusion composition.

Assuming that MI are samples of the original melt trapped during crystallization, the compositions of melt inclusions necessarily represent points on the liquid line of descent for the host rock at the conditions existing in the magma chamber. It follows that a logical approach is to compare the analytical data obtained from MI with phase relationships in systems where the main phases present in the host rock are considered. In our case two systems are of major interest: orthoclase-anorthite-albite (i.e. the ternary feldspar system, OAA, Fig. 4) and anorthite-diopside-albite (ADA, Fig. 5). As noted above, phase diagrams are simplifications of real systems and may not accurately reflect melt evolution in more complicated natural systems. As a consequence, we also present our data on classic Harker variation diagrams (Fig. 6).

There has been extensive experimental and theoretical work on the OAA system (Bowen et al., 1950; Tuttle and Bowen, 1950; Yoder et al., 1957; Seck, 1971, Barron, 1976; Ghiorso, 1984; Furhman and Lindsley, 1988; Wen and Nekvasil, 1994), and the fundamental phase relationships are fairly well known at different pressures. Less information is available for the ADA system. The basic phase relationships in the ADA system were determined by Bowen (1928), who documented the existence of two primary crystallization fields at 1 atm. Barron (1972), using a thermodynamic approach, confirmed Bowen's earlier experimental findings. Lindsley and Emslie (1969) showed that the cotectic boundary between the two primary crystallization fields moves toward compositions richer in anorthite at higher pressure ($> 15 \text{ kb}$).

When plotted in the OAA system, compositions of inclusions from the Ponza trachyte define a fractional crystallization path that extends from a “basaltic” liquid composition towards the trachyte composition (Fig 4). Note that compositions of melt inclusions heated slowly in the heating stage and those heated rapidly in the vertical furnace overlap, indicating that slow heating did not significantly affect the melting behavior or the melt composition as had been reported by Sobolev et al. (1980). As shown schematically in Fig. 7 (modified from Cox et al., 1979), the evolution of a basaltic liquid of composition (B) through fractionation of calcic plagioclase of composition (a) defines a curved path which trends toward the cotectic. At the cotectic, the liquid, now trachytic in composition (P), starts to precipitate K-feldspar of composition (e) in addition to plagioclase with composition (b). The 3 inclusions analyzed in K-feldspar plot away from the inclusions in plagioclase (Fig. 4) which suggests that they did not trap a melt that was co-precipitating plagioclase and K-feldspar. However, the compositions of MI in plagioclase and K-feldspar are similar when plotted on Harker variation diagrams (Fig. 6). Hence, we infer that the differences shown in Fig. 4 are at least partly the result of distortion introduced by projecting the data onto the ternary phase diagram.

Compositions of melt inclusions in pyroxene have been plotted in the ADA system (Fig. 5). According to the phase relationships in this system, these inclusions trapped a liquid which was precipitating a diopsidic pyroxene. This caused the liquid to move away from the diopside apex and towards the pyroxene-plagioclase cotectic curve, a behavior compatible with that observed in the OAA system. This path is represented schematically with a straight line in Fig. 5, but the actual liquid line of descent (LLD) was likely more complicated. The cotectic precipitation of clinopyroxene and plagioclase, while suggested by the trend in Fig. 5 and the partial overlap of MI

data for clinopyroxene and plagioclase in Fig. 6, cannot be unequivocally proved due to the large variability of MI data when plotted in the ADA system.

A precise LLD cannot be constructed owing to the scatter of the data (Fig. 4 and 5) and the lack of more rigorous experimental constraints on phase relationships in the system Albite-Anorthite-Orthoclase-Diopside (AAOD). Nonetheless, a plot of all MI data in this tetrahedron (Fig. 8) is consistent with the interpretation that the parent liquid which produced the trachyte evolved from the Di corner towards the An-Ab-Or side, probably reaching a point along the path where a diopsidic clinopyroxene co-precipitated with an anorthitic feldspar. Once the liquid, now closer in composition to a trachyte than the original basaltic parent, reached the An-Ab-Or side of the tetrahedron, the path moved toward the two-feldspar solvus, crossed it and started to fractionate K-feldspar together with plagioclase.

Data from MI in feldspar have been plotted in the ternary system OAA, as constructed by Barron (1976) and based on data from Seck (1971) at 1 Kb (Fig. 9a). Also shown are compositions of the MI host crystals, and the composition of the Ponza trachyte. MI from high-Ca plagioclase (An_{63} to An_{87}) plot closer to the An-Ab side, whereas MI data from low-Ca plagioclase (An_{46} to An_{55}) cluster near the trachyte composition, together with MI data from K-feldspar. The data from K-feldspar plot between the An_{50} and An_{65} isophase lines (which represent the composition of K-feldspar that would be in equilibrium with plagioclase of a particular An content at a certain temperature) indicating that they co-precipitated with the low-Ca (An_{50} to An_{55}) plagioclase. Moreover the composition of the Ponza Trachyte plots almost exactly on the consolute line (which marks the co-precipitation of K-feldspar and plagioclase). For comparison we also plotted our data on the 2 Kb phase diagram (Fig. 9b; Barron, 1976). At

this higher pressure the consolute line moves towards the An-Ab join and there is poorer agreement between our data and experimental phase relationships, suggesting that pressures during melt entrapment were closer to 1 Kb than 2 Kb. On this diagram K-feldspars plot on the An₄₀ isopleth line and the Ponza Trachyte is far away from the consolute line. All these observations taken together strongly support the hypothesis that the Ponza trachyte evolved from a basaltic parent through fractional crystallization in a shallow magma chamber and that this process played a major role in its evolution, albeit not the only one.

The suggestion that the origin of the trachytic magmas at Ponza is the result of low-pressure differentiation processes in shallow reservoirs is not new (Metrich et al., 1988), and recent geophysical data confirm the existence of an intensely magnetized body that “*could represent the remnant of a shallow magma chamber*” (Orsi et al., 1999). To further test this hypothesis and to identify a possible parent melt for the Ponza trachyte, we have carried out theoretical geochemical modeling using the computer program MELTS (Ghiorso and Sack, 1995). We selected an alkali olivine basalt from the nearby Ventotene island (Tab. 2, VNT3 in: Bellucci et al., 1999) for our starting composition in the MELTS model. The Ponza trachyte and VNT3 are thought to be products of the same magmatic system, and radiometric dating indicates similar ages for these two units (Metrich et al., 1988).

In our model, we constrained the pressure at 1 Kb, as suggested by the agreement between our MI compositions, host crystal compositions and bulk rock data and the phase relations in the Ab-An-Or phase diagram as shown in Fig. 9a. As a starting temperature we selected 1250°C, because this temperature is slightly above the highest temperature required to attain complete melting of crystallized melt inclusions and hence is likely above the liquidus for this composition.

This was confirmed by our runs with MELTS. However, as long as the starting temperature is above the liquidus this temperature choice has no effect on the model results, because MELTS calculates the highest liquidus temperature purely on the basis of the starting composition, pressure and oxygen fugacity. For practical purposes we could have selected any temperature at which we can consider our starting composition to be above the liquidus and the results would not change. In the model, the temperature was decreased in 5°C steps. Oxygen fugacity was constrained along the QFM buffer, assuming that most igneous rocks of this composition equilibrate within a few log units of this buffer (Haggerty, 1976). However, since a few log unit variation in oxygen fugacity could have a large effect on the liquid line of descent, we also investigated the effect of oxygen fugacity on the predicted evolution of the melt.

MELTS predicts a liquidus temperature of 1170°C, at which point the liquid starts precipitating clinopyroxene (Di_{54}) and plagioclase (An_{83}). Clinopyroxene and plagioclase are joined by olivine at 1165°C, by spinel at 1115°C and by K-feldspar at 1030°C. Olivine leaves the liquidus at 1025°C, immediately after K-feldspar crystallization begins. Apatite appears at 1000°C and biotite at 895°C. The model results are summarized in Tab. 2 and Tab. 3. The evolution of the liquid along the liquid line of descent in the ternary feldspar system is shown in Fig. 10b, together with the predicted compositions of the precipitating feldspars. In Fig. 10a the liquid evolution path is compared to the MI data.

Results from the MELTS model, and analytical data from minerals and melt inclusions, agree in many respects, but not in all. MELTS model results and the MI data describe a similar crystallization trend and compositions of feldspars, and the order in which phases crystallize (Tab. 3, 4, Fig. 10a and 10b). However, whereas MELTS predicts a continuous range of plagioclase

compositions (Fig. 10b), data from the trachyte show two gaps in the plagioclase composition, corresponding to $An_{72}-An_{78}$ and $An_{56}-An_{63}$. The gaps in measured compositions of these zoned plagioclases are likely the result of the limited number of analysis.

The MELTS model results and the MI data disagree on two points. MELTS does not reproduce the actual composition of the pyroxenes (Tab. 4). However it is known that the model poorly reproduces pyroxene equilibria (Yang et al., 1996). Additionally, the evolution trend of the liquid composition predicted by MELTS (i.e. the Liquid Line of Descent - LLD) and the one shown by MI data are clearly different. LLD defined by MELTS during plagioclase-only crystallization is displaced toward compositions richer in An and Or, compared to the trend defined by the MI analyses (Fig. 10b). There are a number of possible explanations for these differences, some of which are considered below.

Magmatic systems are complex, and many different physical and chemical factors affect the chemical evolution of magmas. However, theoretical models generally cannot consider all of the many possible combinations that might occur in natural systems, and it is not always possible to analytically determine with a high degree of accuracy all of the parameters that go into a model. For example, we have chosen VNT3 as the starting composition because it belongs to the same magmatic system as the Ponza trachyte. An artificial composition might have produced a closer match with our MI data, but we intended to illustrate how MI data can be combined with a theoretical model in order to constrain the parameters that control magmatic processes in natural systems containing real rocks.

Pressure in the magma chamber can significantly affect the LLD. Geologic information suggests a shallow magma chamber at Ponza, and after comparing MI data with phase equilibria

(Fig. 9a and 9b) determined from experimental data (Seck, 1971), we selected a pressure of 1 Kb for our model. Higher pressures show poorer agreement between model and MI predictions. The oxygen fugacity during MI entrapment is not well constrained, and we selected QFM for our model. Changing f_{O_2} one or two log units below the QFM buffer has an insignificant effect on the plagioclase-only part of the LLD, while the co-precipitation of K-feldspar and plagioclase was shifted to slightly lower temperatures and compositions richer in anorthite (Fig. 10c). The H_2O content of the melts is not well known, and we used a value of 0.3 wt. % for the starting melt in our model. Increasing the initial water content in the VNT3 sample to 1 wt. % (Fig. 10d) caused a slight shift of the plagioclase-only part of the LLD toward compositions richer in Ab. However, this part of the LLD still differs from the trend defined by MI data. A further increase of the initial water content would have produced an even greater shift of the LLD predicted by MELTS towards the MI trend, but we have no evidence of high water content in the melts (i.e. no evidence of magmatic aqueous inclusions).

Concentrations of oxide components from melt inclusions are plotted against the Solidification Index ($SI = [100 \times MgO/(MgO+FeO+Fe_2O_3+Na_2O+K_2O)]$) together with the MELTS-modeled evolution of the Ventotene AOB (Fig. 11). Although there is some scatter of the data, MI analyses agree with the modeled trends for SiO_2 , FeO , MnO , MgO , Na_2O , K_2O and CaO , with a major discrepancy only for TiO_2 and Al_2O_3 . The behavior of Al_2O_3 is especially anomalous when compared with the trend produced by MELTS. A possible explanation is that melt inclusions in more evolved plagioclase were modified by excess re-melting of the host during heating. Indeed late plagioclase hosts (i.e. formed at lower temperatures) would be more

susceptible to melting at the temperatures of the re-melting experiments. We have calculated the effect of excess host re-melting by subtracting 25% of the host composition from MI analysis and report a few examples calculations in Table 6. It is worth noting that these plots also show that some MI in clinopyroxene presumably record the melt evolution before the point where our modeling starts. In fact even after correction for apatite contamination, some MI in clinopyroxene still have SI about 30 (Tab. 5).

Based on the data from MI and the results from MELTS, we suggest a genetic link between the trachyte and the Ventotene alkali-olivine basalt (VNT3), consistent with earlier interpretations. As is clearly shown in Fig. 4, 5, 9, 10 and Table 3, fractional crystallization of VNT3 at 1 Kb produces both the phases found in the trachyte and a crystallization trend parallel to the one recorded by MI, while the data in Fig. 11 confirm the close match between the compositional data obtained by MI and that predicted by MELTS modeling. The difference between the crystallization path obtained by MI data and the one produced by MELTS as plotted in Fig. 10a, could be explained by the following:

- 1) As shown in Fig. 11, VNT3 is genetically linked to the Ponza trachyte but it is not the primary magma that generated the trachyte. This parent magma likely had a different composition represented by the MI compositions in pyroxene and it might have followed a slightly different LLD.

- 2) MELTS was designed to reproduce melt evolution in a multi-component system (Ghiorso and Sack, 1995) and plots in Fig. 10 represent an extrapolation of the results obtained through MELTS modeling to a three component system. This forces the

mathematical model into unfamiliar territory and, while preserving the general trend for the LLD, could explain the discrepancy observed in Fig. 10a.

3) There are uncertainties connected to the MI data, which might be due to under-melting or over-melting of the plagioclase and clinopyroxene hosts or to other magmatic processes superimposed on the fractional crystallization process. These factors cannot be quantified with the data available.

Conclusions

The origin of the Ponza trachyte was investigated by combining compositional data obtained from MI with compositional trends predicted by theoretical modeling using the program MELTS. MI were re-heated to obtain an homogeneous glass before analysis. This was done using two different techniques, slow heating in a heating stage and fast heating in a vertical furnace, with the purpose of identifying possible effects of heating rates on MI compositions. No detectable effect was found. MI data were compared with known phase relations in the ternary feldspar and anorthite-diopside-albite systems to constrain the physical parameters used in the modeling.

MI data are consistent with melt evolution from a basaltic parent via a fractional crystallization process, which was controlled mainly by crystallization of pyroxene and feldspars, but cannot exclude substantial contributions from other magmatic processes. These data, in conjunction with results from MELTS, are consistent with a genetic link between the Ponza trachyte and the coeval and co-magmatic alkali olivine basalts (VNT3) on the nearby Ventotene Island.

References

- Anderson A.T. (1974) Evidence for a picritic, volatile-rich magma beneath Mt. Shasta, California. *J. Petrol.* 15:243-267.
- Bacon C. R. (1989) Crystallization of accessory phases in magmas by local saturation adjacent to phenocrysts. *Geochim. Cosmochim. Acta* 53:1055-1066.
- Barberi F., Gasparini P., Innocenti F. and Villari L. (1973) Volcanism of the Southern Tyrrhenian Sea and its Geodynamic Implications. *J. Geophys. Res.*, 78:5221-5232.
- Barron L. M. (1972) Thermodynamic Multicomponent Silicate Equilibrium Phase Calculations. *Am. Mineral.* 57:809-823.
- Barron L. M. (1976) A Comparison of Two Models of Ternary Excess Free Energy. *Contrib. Mineral. Petrol.* 57:71-81.
- Bassi G., Sabadini R. and Rebai S. (1997) Modern Tectonic Regime in the Tyrrhenian Area: Observations and Models. *Geophys. J. Int.* 129:330-346.
- Bellucci F., Lirer R. and Munno R. (1999) Geology of Ponza, Ventotene and Santo Stefano Islands (with a 1:15,000 scale geological map). *Acta Vulcanol.* 11(2):197-222.
- Boccaletti M. and Guazzone G. (1972) Evoluzione Paleogeografica e Geodinamica del Mediterraneo: I Bacini Marginali. *Mem. Soc. Geol. It.*, 13:162-169.
- Bodnar R.J and Bethke P.M. (1984) Systematics of stretching of fluid inclusions. I. Fluorite and sphalerite at 1 atmosphere confining pressure. *Econ. Geol.* 79:141-161.
- Bowen N. L. (1928) *The Evolution of the Igneous Rocks*. Princeton University Press, Princeton, N.J.
- Bowen N. L. and Tuttle O. F. (1950) The system $\text{NaAlSi}_3\text{O}_8 - \text{KAlSi}_3\text{O}_8 - \text{H}_2\text{O}$. *Journal of Geology*, 58(5):489-511.
- Conte A. M and Dolfi D. (2002) Petrological and Geochemical Characteristics of Plio-Pleistocene Volcanics from Ponza Island (Tyrrhenian Sea, Italy). *Mineral. Petrol.*, 74:75-94.
- Cox K. G., Bell J. D. and Pankhurst R. J. (1979) *The Interpretation of Igneous Rocks*. Unwin Hyman, London, 450 pp.
- Danyushevsky L. V., McNeill A. W. and Sobolev A. V. (2002) Experimental and Petrological studies of melt inclusions in phenocrysts from mantle-derived magmas: an overview of techniques, advantages and complications. *Chem. Geol.* (In Press).
- Frezzotti M. L. (2001) Silicate-melt inclusions in magmatic rocks: application to petrology. *Lithos* 55:273-299.
- Furhman M. L. and Lindsley D. H. (1988) Ternary-feldspar modeling and thermometry. *Am. Mineral.* 73:201-215.

- Ghiorso M. S. (1984) Activity/composition relations in the ternary feldspars. *Contrib. Mineral. Petrol.* 87(3):282-296.
- Ghiorso, M. S., and Sack, R. O. (1995) Chemical Mass Transfer in Magmatic Processes. IV. A Revised and Internally Consistent Thermodynamic Model for the Interpolation and Extrapolation of Liquid-Solid Equilibria in Magmatic Systems at Elevated Temperatures and Pressures. *Contributions to Mineralogy and Petrology*, 119:197-212.
- Haggerty S. E. (1976) Opaque mineral oxides in terrestrial igneous rocks. *Rev. Mineral.* 3, Hg101-Hg300. Mineralogical Society of America.
- Halter W., Pettke T., Heinrich C. A. and Rothen-Rutishauser B. (2002) Major to trace element analysis of melt inclusions by laser-ablation ICP-MS: methods of quantification. *Chem. Geol.* In Press.
- Hari K. R., Santosh M. and Chatterjee A. C. (1991) Primary Silicate-melt Inclusions in Olivine Phenocrysts from the Pavagad Igneous Suite, Gujarat. *J. Geol. Soc. India*, 37:343-350.
- Laubscher H. P. (1975) Plate Boundaries and Microplates in Alpine History. *Am. J. Sci.* 275:865-876.
- Lavecchia G. and Stoppa F. (1996) The Tectonic Significance of Italian Magmatism: an Alternative View to the Popular Interpretation. *Terra Nova* 8:435-446.
- Lindsley D. H. and Emslie R. F. (1968) Effect of Pressure on the Boundary Curve in the System Diopside-Albite-Anorthite. *Carnegie Inst. Wash., Year Book.* 66:479-480.
- Locardi E. (1982) Individuazione di Strutture sismogenetiche dall'esame dell'evoluzione vulcano-tettonica dell'Appennino e del Tirreno. *Mem. Soc. Geol. Ital.* 34:569-596.
- Lowenstern J. B. (1994) Chlorine, fluid immiscibility and degassing in peralkaline magmas from Pantelleria, Italy. *Am. Mineral.* 79:353-369.
- Lowenstern J.B. (1995) Applications of Silicate-Melt Inclusions to the Study of Magmatic Volatiles, in: J.F.H Thompson, *Fluids and Ore Deposition*, Mineral. Assoc. Canada, Short Course Series 23:71-99.
- Lu F., Anderson A.T. and Davis A.M. (1995) Diffusional gradients at the crystal/melt interface and their effect on the compositions of melt inclusions. *J. Geol.* 103:591-597.
- Metrich N., Santacroce R. and Savelli C. (1988) Ventotene, a potassic Quaternary volcano in Central Tyrrhenian Sea. *Rend. Soc. It. Mineral. Petrol.*, 43:1195-1213.
- Nielsen R. L., Crum J., Bourgeois R., Hascall K., Forsythe L. M, Fisk M. R. and Christie D. M. (1995) Melt inclusions in high-An plagioclase from the Gorda Ridge: an example of the local diversity of MORB parent magmas. *Contrib. Mineral. Petrol.* 122:34-50.
- Nielsen R. L., Michael P. J. and Sours-Page R. (1998) Chemical and physical indicators of compromised melt inclusions. *Geochim. et Cosmochim. Acta.* 62(5):831-839.

- Orsi G., Patella D., Piochi M. and Tramacere A. (1999) Magnetic modeling of the Phlegraean Volcanic District with extension to the Ponza archipelago, Italy. *J. Volc. Geoth. Res.*, 91:345-360.
- Patacca E., Sartori R. and Scandone P. (1990) Tyrrhenian basin and Apeninonic Arcs: Kinematic relations since late Tortonian times. *Mem. Soc. Geol. Ital.* 45:425-451.
- Pozzuoli A. (1988) Mineralogy, Geochemistry and Origin of Alteration Products in the Pontian Archipelago (Italy): 1 - The Genesis of the Ponza Bentonite. 10th Conference on Clay Mineralogy and Petrology, Ostrava 89-98.
- Qin Z., Lu F. and Anderson A. T. Jr. (1992) Diffusive reequilibration of melt and fluid inclusions. *Am. Mineral.* 77:565-576.
- Raia F., Webster J. D. and De Vivo B. (2000) Pre-eruptive volatile contents of Vesuvius magmas: constraints on eruptive history and behavior. I – The medieval and modern interplinian activities. *Eur. J. Mineral.* 12:179-193.
- Roedder, E., (1979) Origin and significance of magmatic inclusions. *Bull. Minéral.* 102, 487-510.
- Roedder E. (1984) Fluid Inclusions, *Min. Soc. Am. Rev. in Min.* v. 12, 646 pp.
- Savelli D. and Wezel F.C. (1979) Morfologia e stile tettonico del Bacino Tirrenico. *Atti Conv. Sc. Naz. P.F. Oceanografia e Fondi Marini CNR Roma.* 2:729-738.
- Scandone P., Origin of the Tyrrhenian Sea and Calabrian Arc. *Boll. Soc. Geol. It.*, (1980) 98:27-34.
- Seck H. A. (1971) Koexistierende Alkalifelspate und Plagioklase im System $\text{NaAlSi}_3\text{O}_8$ - KAlSi_3O_8 - $\text{CaAl}_2\text{Si}_2\text{O}_8$ - H_2O bei Temperaturen von 650 °C bis 900 °C. *Neues Jahrbuch für Mineralogie Abhandlungen*, 115:315-345.
- Sinton C. W., Christie D. M., Coombs V. L., Nielsen R. L. and Fisk M. R. (1993) Near-primary melt inclusions in anorthite phenocrysts from the Galapagos Platform. *Earth. Planet. Sci. Lett.* 119:527-537.
- Skirius C. M., Peterson J. W. and Anderson A. T. Jr. (1990) Homogenizing rhyolitic glass inclusions from the Bishop Tuff. *Am. Mineral.* 75:1381-1398.
- Sobolev A. V. (1996) Melt inclusions in minerals as a source of principal petrologic information. *Petrology*, 4:228-239.
- Sobolev A.V., Dmitriev L.V., Barsukov V.L., Nevzorov V.N. and Slutsky A.B. (1980) The formation conditions of high magnesium olivines from the mono-mineral fraction of Luna-24 regolith. 11th Lunar and Planet. Sci. Conf., pp. 105-116.
- Stanley D. J. and Wezel F. C. (1985) *Geological Evolution of the Mediterranean Basin.* Springer-Verlag, New York, 589 pp.
- Student J.J. and Bodnar R.J. (1999) Synthetic Fluid Inclusions XIV: Microthermometric and compositional analysis of coexisting silicate melt and aqueous fluid inclusions trapped in the

- haplogranite-H₂O-NaCl-KCl system at 800 °C and 2000 bars. *Journal of Petrology*, 40:1509-1525.
- Thomas J.B., Bodnar J.B., Shimizu N. and Chesner C. (2001) The role of boundary layers during entrapment of melt inclusions: evidence from the Toba Tuffs Sumatra, Indonesia. *EOS Trans. AGU*, 82 (47), Fall Meeting Suppl. Abs. V32D-1014.
- Thomas J.B., Shimizu N, Sinha A.K. and Bodnar R.J. (2000) Melt Inclusions in zircon as recorders of melt evolution in crystallizing granitic plutons. *Geol. Soc. Of America, Program & Abstracts*, A398.
- Thomas R. and Webster J.D. (2000) Strong tin enrichment in a pegmatite-forming melt. *Min. Deposita*, 35:570-582.
- Turco E. and Zuppetta A. (1998) A Kinematic Model for the Plio-Quaternary Evolution of the Tyrrhenian-Apenninica System: Implications for Rifting Processes and Volcanism. *J. Volcan. Geoth. Res.* 82:1-18.
- Tuttle O. F. and Bowen N. L. (1950) High-temperature albite and contiguous feldspars. *Journal of Geology*, 58(5):572-583.
- Ulrich M.R. and Bodnar R.J. (1988) Systematics of stretching fluid inclusions. II. Barite at one atmosphere confining pressure. *Econ. Geol.* 83:1037-1046.
- Watson E. B., Sneering M. A. and Ross A. (1982) Diffusion of dissolved carbonate in magmas: experimental results and applications. *Earth. Planet. Sci. Lett.* 61:346-358.
- Wen S. and Nekvasil H. (1994) Solvcalc: an Interactive Graphics Program Package for Calculating the Ternary Feldspar Solvus and for Two-feldspar Geothermometry. *Computers & Geosciences*, 20(6):1025-1040.
- Yang H., Kinzler J.K. and Grove T.L. (1996) Experiments and models of anhydrous, basaltic olivine-plagioclase-augite saturated melts from 0.001 to 10 Kbar. *Contrib. Mineral. Petrol.* 124:1-18.
- Yang K. and Bodnar R.J. (1994) Magmatic-hydrothermal evolution in the “bottoms” of porphyry copper systems: Evidence from silicate melt and aqueous fluid inclusions in granitoid intrusions in the Gyeongsang Basin, South Korea. *Int. Geol. Rev.* 36: 608-628.
- Ylagan R. F., Altaner S. P. and Pozzuoli A. (1996) Hydrothermal Alteration of a Rhyolitic Hyaloclastite from Ponza Island, Italy. *J. Volcan. Geoth. Res.* 74:215-231.
- Yoder H. S., Stewart D. B. and Smith J. R. (1957) Ternary Feldspars. *Carnegie Inst. Wash., Year Book.* 56:207-214.

CHAPTER 2

Application of the olivine-spinel geothermometer to volcanic rocks: An example from Tahitian Basanite.

Spinel-silicate equilibria may be very useful as petrogenetic indicators due to the wide compositional range and the sensitivity to temperature, bulk composition and f_{O_2} of spinel (Irvine, 1965). However, thermometric applications have been mainly confined to plutonic rocks, although the spinel-silicate association is common in mafic volcanic rocks as well. In particular, the pair olivine-spinel commonly occurs in basaltic (broadly defined) lava flows and shallow intrusions (dikes and sills). In this study we have applied olivine-spinel thermometry to samples from a basanite dike collected from Tahiti.

The island of Tahiti is located west of the East Pacific Rise and is part of the Society Islands volcanic chain. During most of the Cenozoic it has been quite active, producing “what is probably the most complete suite of strongly alkaline rocks in the Pacific Ocean” (McBirney and Aoki, 1968). The basanite samples we investigated were collected in 1968 from boulders in the bed of Fatauaa River near Papeete and their petrology has been thoroughly described by Tracy and Robinson (1977). The basanite is notable due to the presence of a suite of ultramafic nodules (dunites, wehrlites and lherzolites) which are a relatively rare occurrence in Tahiti and have been studied in detail (Tracy, 1980).

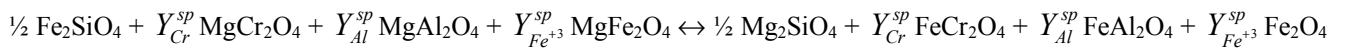
Observation of the basanite in thin section reveals the presence of olivine, titanite, plagioclase and titanomagnetite as abundant phenocrysts. Minor alkali feldspar, leucite, apatite, ilmenite and small patches of glass or devitrified glass are also present in matrix. Zoned olivine phenocrysts commonly incorporate small (from 2 to 15 μm in major axis length) euhedral to subhedral spinel inclusions which display different reflectivities, depending on core-to-rim

location, and suggest systematic variations in composition of spinel and entrapping olivine. This motivated us to investigate Fe-Mg fractionation between olivine phenocrysts and associated spinel inclusions to test the applicability of the olivine-spinel geothermometer to this rock and to assess the T range of the crystallization history of the basanite.

Using microprobe analysis of olivine-spinel pairs found within olivine phenocrysts, we applied different calibrations and thermodynamic models of the olivine-spinel geothermometer (Irvine, 1965; Roeder et al, 1979; Sack and Ghiorso, 1991b; Jianping et al., 1995) in order to evaluate the systematics of olivine-spinel Fe-Mg partitioning in these samples and to assess the temperature dependence of this partitioning.

The Olivine-Spinel Geothermometer.

Irvine (1965) described how the pair magnesian olivine + Cr-Al-spinel can be used as a geothermometer, pointing out that the distribution of Fe⁺² and Mg between these two phases is very sensitive to temperature, in particular for Cr-rich spinels. Considering only the six predominant end-members of the spinel series (i.e. those used in the spinel compositional prism), the Mg-Fe⁺² exchange can be expressed with the following reaction:



where $Y_i^{sp} = N_i^{sp} / (N_{Cr}^{sp} + N_{Al}^{sp} + N_{Fe^{+3}}^{sp})$ and N_i^{sp} is the mole fraction of component i in the spinel.

Irvine (1965) showed that under the reasonable, albeit restrictive, assumption that “chromian spinel solid solutions are ideal over their natural range of compositions at the temperatures of

basaltic magmas”, it is possible to reach a simple formulation of the distribution coefficient for Mg and Fe⁺²:

$$K_d = \frac{X_{Mg}^{ol} \times X_{Fe^{+2}}^{sp}}{X_{Fe^{+2}}^{ol} \times X_{Mg}^{sp}}$$

The geothermometer has been successfully calibrated and applied to plutonic rocks (Jackson, 1969) but some authors have noted that when applied to volcanic assemblages, calculated temperatures were geologically unrealistic (Evans and Wright, 1972). Roeder et al. (1979) re-evaluated the geothermometer and proved that it can be used to calculate realistic magmatic temperatures for volcanic rocks providing that a different value of the Gibbs free energy is used for FeCr₂O₄. They proposed the following relationship:

$$T(^{\circ}K) = \frac{\alpha 3480 + \beta 1018 - \gamma 1720 + 2400}{\alpha 2.23 + \beta 2.56 - \gamma 3.08 - 1.47 + 1.987 \ln K_d}$$

where $\alpha = Cr/(Cr + Al + Fe^{+3})$; $\beta = Al/(Cr + Al + Fe^{+3})$; $\gamma = Fe^{+3}/(Cr + Al + Fe^{+3})$.

More recently, Jianping et al. (1995) proposed a new relationship based on their experimental data and on a solid solution model for spinels developed by Wood and Nicholls (1978), in an attempt to reconcile the temperatures obtained from the olivine-spinel geothermometer with those obtained with geothermometers based upon Ca or Al content in pyroxenes:

$$T(^{\circ}K) = \frac{4299Y_{Cr}^{sp} + 1283}{1.469Y_{Cr}^{sp} - 2Y_{Fe^{+3}}^{sp} + 0.363 + \ln K_d}$$

A more complex model for the spinel solid solution and the equilibrium olivine-spinel has been proposed by Sack and Ghiorso (1991b) as part of their program to develop thermodynamic models for standard state and mixing properties of common rock forming minerals based on internally consistent thermodynamic datasets. The model is an extension of that proposed by Sack and Ghiorso (1991a) for Cr-free spinels and uses the following simplifications:

- 1) cations exhibit only long-range, non-convergent ordering between tetrahedral and octahedral sites.
- 2) the vibrational Gibbs free energy may be described by a Taylor expansion of second degree for seven linearly independent variables of composition and ordering.
- 3) there are no excess vibrational entropies of mixing.

Olivine-spinel data from the basanite

More than 100 olivine-spinel pairs have been analyzed in thin sections from the basanite, using a Cameca SX50 microprobe in the Department of Geological Sciences at Virginia Tech. Analytical conditions were 15 Kv and 20 nA, counting time of 20 sec. for all elements. Calibrations were done on natural and synthetic oxides. Fe₂O₃ in spinel was calculated by using the assumptions of charge balance and spinel stoichiometry, i.e. 3 cations per 4 oxygens (Table 1).

All analyzed spinels occur as inclusions (commonly euhedral) within olivine phenocrysts, have maximum dimension from 2 to 15 μm , and range in composition from Cr-rich in olivine cores to Cr- and Al-poor and Ti-rich at olivine rims (Fig. 1). Only the trapping in phenocrysts (olivine and pyroxene in this rock) allows the preservation of this wide range of transient spinel

OLIVINE									SPINEL								
	SiO2	TiO2	Al2O3	Cr2O3	MgO	MnO	FeO	Total	SiO2	TiO2	Al2O3	Cr2O3	MgO	MnO	FeO	Fe2O3	TOTAL
1	40.93	0.00	0.05	0.07	45.51	0.21	14.15	100.93	0.09	26.32	5.04	0.05	3.91	0.78	41.75	23.10	101.04
2	40.20	0.01	0.06	0.08	43.56	0.26	16.78	100.96	0.42	2.37	23.98	29.42	10.61	n.d	20.65	12.50	99.95
3	38.46	0.20	0.04	0.09	37.16	0.41	24.17	100.54	0.04	23.83	7.36	4.45	4.44	0.51	40.65	17.93	99.21
4	39.00	0.04	0.04	0.05	40.85	0.29	18.96	99.22	0.10	2.61	22.11	29.06	9.68	n.d	21.50	13.34	98.41
5	38.65	0.05	0.12	0.04	41.20	0.31	18.46	98.82	0.42	7.90	30.97	14.47	11.66	n.d	23.71	10.25	99.37
6	38.06	0.05	0.05	0.05	36.91	0.35	24.12	99.59	0.06	23.17	6.83	3.91	4.21	0.51	39.54	20.08	98.31
7	38.56	0.03	0.04	0.03	38.71	0.34	20.16	97.86	0.27	3.46	17.57	27.85	8.10	n.d	22.66	15.81	95.72
8	39.13	0.02	0.04	0.07	40.52	0.25	18.73	98.76	0.08	2.36	21.85	27.12	9.00	n.d	21.68	14.37	96.46
9	38.39	0.02	0.03	0.11	39.21	0.32	21.15	99.22	0.10	3.40	17.22	28.08	8.14	n.d	22.60	16.45	95.96
10	38.20	0.01	0.05	0.04	38.02	0.37	22.05	98.74	0.48	2.86	18.73	26.06	7.99	n.d	22.76	17.63	96.51
11	35.89	0.19	1.46	1.59	37.82	0.25	20.99	98.18	0.13	2.17	22.07	28.07	9.10	n.d	21.84	14.28	97.66
12	39.14	0.00	0.06	0.08	42.24	0.28	17.68	99.47	0.90	5.26	17.96	24.55	10.02	n.d	20.94	18.21	97.83
13	38.95	0.03	0.07	0.05	41.79	0.24	17.70	98.82	0.52	2.32	22.42	29.20	10.77	n.d	19.70	14.11	99.02
14	39.51	0.00	0.05	0.10	42.42	0.26	18.16	100.50	0.12	3.09	23.20	27.91	9.05	n.d	23.15	12.27	98.78
15	39.05	0.01	0.05	0.04	38.93	0.36	23.24	101.69	0.45	10.03	16.54	20.75	7.17	n.d	29.26	15.25	99.44
16	37.08	0.15	0.14	0.02	36.81	0.45	23.67	98.31	0.11	12.87	12.37	11.89	7.73	0.07	27.09	25.29	97.42
17	38.09	0.07	0.06	0.03	37.01	0.40	23.98	99.63	0.20	10.87	13.34	14.39	6.81	0.00	28.26	24.62	98.48
18	38.94	0.04	0.05	0.03	39.83	0.26	20.89	100.04	0.34	3.71	17.99	28.35	8.41	0.00	22.97	15.85	97.61
19	37.70	0.08	0.02	0.03	35.52	0.46	26.22	100.03	0.07	11.55	13.06	12.53	5.36	0.04	30.87	24.60	98.08
20	37.63	0.06	0.06	0.07	35.38	0.38	26.39	99.96	0.08	4.08	17.18	25.25	6.61	0.33	25.42	18.58	97.52
21	38.42	0.10	0.03	0.04	37.51	0.39	23.68	100.17	0.08	13.36	11.18	10.14	6.90	0.42	27.94	27.73	97.75
22	39.17	0.01	0.05	0.02	40.76	0.29	19.72	100.02	0.09	10.97	15.14	12.20	8.32	0.33	25.53	25.71	98.29
23	38.89	0.05	0.02	0.11	39.46	0.36	21.60	100.48	0.04	2.97	19.49	28.69	8.54	0.34	22.79	16.20	99.05
24	39.65	0.04	0.03	0.06	42.83	0.22	17.36	100.18	0.09	2.64	21.44	29.99	10.19	0.26	20.35	13.52	98.48
25	39.67	0.02	0.04	0.07	42.87	0.20	17.21	100.08	0.12	2.82	21.75	30.59	10.76	0.27	19.87	13.06	99.24
26	39.67	0.02	0.04	0.07	42.87	0.20	17.21	100.08	0.15	2.96	24.21	28.68	11.64	0.25	19.00	12.26	99.14
27	38.40	0.05	0.05	0.03	39.53	0.34	20.86	99.27	0.09	10.82	13.70	13.92	8.14	0.34	25.65	26.24	98.91
28	37.93	0.03	0.04	0.02	36.67	0.39	24.46	99.55	0.93	11.13	13.51	12.37	6.89	0.40	27.54	26.17	98.95
29	37.73	0.05	0.05	0.07	36.57	0.38	24.19	99.03	0.07	3.37	17.73	28.17	7.06	0.44	24.66	16.76	98.26
30	38.66	0.05	0.05	0.06	41.29	0.28	19.14	99.52	0.11	6.74	17.45	26.17	8.73	0.33	24.19	14.36	98.09
31	36.81	0.34	0.05	0.05	32.55	0.57	29.57	99.93	0.09	21.65	7.39	6.81	3.74	0.62	39.83	19.00	99.12
32	37.56	0.07	0.04	0.05	35.69	0.43	26.09	99.92	0.07	26.09	5.03	0.63	3.03	0.64	43.46	20.64	99.59
33	38.26	0.03	0.06	0.09	37.92	0.32	22.58	99.26	0.14	3.28	18.22	28.63	8.19	0.35	23.21	16.99	99.01
34	38.26	0.03	0.06	0.09	37.92	0.32	22.58	99.26	0.26	3.28	17.98	26.93	7.43	0.38	24.23	18.61	99.11
35	38.07	0.06	0.05	0.10	39.46	0.30	21.46	99.51	0.10	2.81	19.05	29.12	8.52	0.32	22.51	16.12	98.56
36	36.99	0.11	0.04	0.00	36.12	0.41	25.30	98.96	0.12	3.35	18.27	26.03	6.62	0.38	25.29	17.86	97.93
37	37.10	0.11	0.05	0.03	35.33	0.40	26.15	99.19	0.05	25.27	5.19	0.13	5.15	0.55	37.95	24.55	98.83
38	36.39	0.17	0.03	0.01	33.90	0.43	27.79	98.73	0.07	25.53	5.31	0.37	3.61	0.68	41.54	22.46	99.56
39	38.15	0.00	0.06	0.02	40.27	0.31	19.86	98.67	0.22	2.23	18.99	30.96	8.94	0.35	21.42	15.25	98.36
40	38.30	0.01	0.03	0.06	40.60	0.28	20.24	99.51	0.09	5.37	17.17	23.13	8.98	0.24	22.70	21.31	98.99
41	38.46	0.06	0.05	0.06	41.29	0.23	18.97	99.12	0.10	2.71	19.30	29.80	9.25	0.33	21.24	15.47	98.19
42	36.73	0.42	0.03	0.03	33.28	0.50	28.78	99.76	0.08	25.25	5.48	1.05	3.50	0.68	41.67	21.07	98.77
43	37.96	0.18	0.05	0.04	37.72	0.39	23.19	99.51	0.22	12.35	12.79	10.80	6.99	0.40	28.15	27.87	99.57
44	36.63	0.09	0.05	0.00	32.91	0.44	28.91	99.02	0.13	17.36	11.77	13.40	4.96	0.58	36.59	12.90	97.69
45	38.48	0.05	0.03	0.07	42.62	0.15	17.33	98.73	0.08	3.32	21.40	30.09	10.45	0.33	20.51	12.93	99.10
46	38.38	0.04	0.05	0.09	42.70	0.28	17.13	98.68	0.13	7.43	18.89	23.36	10.35	0.37	22.13	15.92	98.57
47	37.77	0.03	0.03	0.02	39.68	0.31	20.97	98.80	0.35	15.14	9.94	6.73	7.50	0.35	27.30	30.93	98.24
48	38.23	0.05	0.03	0.04	41.43	0.23	18.43	98.44	0.17	2.36	22.03	30.58	10.27	0.27	20.28	12.87	98.82
49	38.23	0.05	0.03	0.04	41.43	0.23	18.43	98.44	0.28	3.21	19.03	30.06	9.36	0.34	21.61	15.43	99.32
50	37.71	0.06	0.04	0.02	38.29	0.36	22.62	99.09	0.11	20.55	9.10	2.56	6.17	0.37	33.52	26.12	98.50
51	37.71	0.06	0.04	0.02	38.29	0.36	22.62	99.09	0.08	20.93	8.81	2.13	6.20	0.48	33.56	26.79	98.98
52	37.71	0.06	0.04	0.02	38.29	0.36	22.62	99.09	0.27	21.39	7.68	3.74	4.39	0.57	37.25	22.72	98.01

Tab. 1 – Olivine and Spinel data.

		OLIVINE								SPINEL								
		SiO2	TiO2	Al2O3	Cr2O3	MgO	MnO	FeO	Total	SiO2	TiO2	Al2O3	Cr2O3	MgO	MnO	FeO	Fe2O3	TOTAL
53		38.16	0.04	0.04	0.11	40.44	0.32	20.07	99.17	0.05	10.63	13.53	13.81	8.17	0.34	24.83	25.41	96.78
54		38.14	0.03	0.08	0.03	38.74	0.33	21.14	98.49	0.13	3.97	18.21	28.62	8.30	0.30	23.51	15.85	98.87
55		38.74	0.02	0.06	0.07	42.55	0.21	17.54	99.19	0.13	2.64	20.91	29.85	10.29	0.32	19.89	14.08	98.11
56		38.94	0.03	0.06	0.08	43.23	0.22	16.92	99.48	0.14	1.83	25.02	29.68	11.31	0.32	18.68	11.27	98.25
57		38.44	0.06	0.04	0.10	38.27	0.34	21.90	99.15	0.12	7.22	15.99	20.69	8.46	0.35	23.71	20.95	97.49
58		39.20	0.02	0.07	0.16	41.25	0.28	18.74	99.71	0.07	2.69	21.10	28.52	9.44	0.31	21.05	14.14	97.31
59		38.42	0.02	0.05	0.07	38.20	0.32	22.44	99.52	0.11	3.05	18.31	26.66	7.61	0.38	23.32	17.67	97.11
60		37.00	0.11	0.06	0.00	32.70	0.44	29.08	99.38	0.09	26.58	4.54	0.10	3.23	0.67	43.06	20.14	98.40
61		39.74	0.04	0.05	0.05	43.69	0.24	15.70	99.52	0.06	3.29	21.75	28.66	10.74	0.25	19.65	13.20	97.59
62		39.46	0.03	0.04	0.11	42.20	0.26	17.05	99.15	0.10	3.50	21.56	29.25	10.28	0.32	20.57	12.35	97.92
63		38.71	0.06	0.02	0.10	38.70	0.27	21.80	99.66	0.06	4.91	13.94	28.05	7.12	0.42	24.34	18.24	97.08
64		38.62	0.03	0.04	0.12	38.64	0.35	21.86	99.66	0.08	3.17	18.51	27.78	7.99	0.31	23.08	16.52	97.45
65		35.86	0.42	1.50	1.39	33.21	0.42	26.86	99.66	0.09	5.54	16.03	22.43	6.24	0.35	26.03	19.16	95.87
66		37.40	0.07	0.02	0.00	33.07	0.57	28.58	99.71	0.08	25.92	4.27	0.49	2.71	0.72	43.00	20.36	97.55
67		38.14	0.11	0.04	0.08	36.95	0.33	24.02	99.67	0.52	8.90	13.93	16.46	6.37	0.41	27.32	23.97	97.89
68		38.14	0.11	0.04	0.08	36.95	0.33	24.02	99.67	0.48	10.82	13.18	13.59	6.95	0.43	27.36	26.13	98.94
69		39.12	0.12	0.03	0.11	40.28	0.33	20.14	100.13	0.11	16.12	9.29	6.18	7.82	0.45	27.22	31.76	98.96
70		38.75	0.04	0.05	0.07	40.05	0.29	20.14	99.39	0.20	2.93	17.68	29.36	8.60	0.32	21.55	15.93	96.57
71		38.32	0.03	0.04	0.04	39.20	0.37	21.55	99.55	0.51	9.16	17.64	23.99	8.33	0.40	26.55	10.75	97.33
72		39.40	0.02	0.04	0.07	42.23	0.20	17.19	99.15	0.10	5.47	21.83	26.25	10.06	0.29	22.11	11.09	97.18
73		37.86	0.07	0.05	0.06	36.90	0.39	22.67	98.00	0.06	17.57	9.76	10.09	4.43	0.54	35.55	18.44	96.44
74		38.88	0.06	0.03	0.12	40.27	0.34	19.16	98.86	0.07	3.01	20.64	28.23	9.33	0.27	21.25	14.17	96.97
75		37.45	0.03	0.06	0.10	39.11	0.31	20.89	97.94	0.13	2.24	21.24	29.33	8.80	n.d	21.98	13.58	97.30
76		36.54	0.10	0.58	0.68	39.32	0.28	19.55	97.06	0.08	3.11	19.23	29.65	8.25	n.d	23.06	14.35	97.71
77		37.57	0.62	0.04	0.11	38.14	0.33	21.25	98.06	0.12	3.71	17.29	27.81	7.01	n.d	24.82	16.20	96.96
78		37.92	0.07	0.07	0.04	40.18	0.30	18.57	97.14	0.58	3.02	19.04	28.87	8.40	n.d	22.41	14.16	96.49
79		36.63	0.11	0.03	0.03	33.99	0.41	26.56	97.76	0.09	26.31	4.35	1.09	2.90	0.69	43.59	19.36	98.38
80		37.97	0.00	0.05	0.00	39.19	0.33	20.14	97.68	0.08	11.97	13.06	12.69	7.18	0.21	27.57	24.74	97.50
81		38.14	0.02	0.05	0.14	40.13	0.30	18.77	97.55	0.11	3.69	21.11	27.02	8.68	n.d	23.36	14.09	98.06
82		38.07	0.04	0.05	0.11	39.06	0.28	20.64	98.25	0.10	3.72	20.06	27.12	8.33	n.d	23.52	14.82	97.67
83		38.01	0.06	0.05	0.10	38.98	0.26	21.00	98.47	0.10	3.18	18.03	29.21	7.54	n.d	24.01	15.34	97.41
84		37.65	0.02	0.06	0.07	40.92	0.24	18.61	97.56	0.12	2.48	20.85	29.70	9.01	n.d	21.75	13.00	96.91
85		38.15	0.06	0.06	0.00	41.47	0.23	17.89	97.86	0.08	13.51	16.60	9.43	9.02	0.22	26.21	22.54	97.61
86		36.42	0.15	0.03	0.01	34.58	0.50	26.75	98.43	0.10	24.92	5.95	2.22	3.50	0.65	41.96	18.92	98.21
87		37.81	0.02	0.04	0.09	38.11	0.36	21.68	98.11	0.11	2.84	19.23	29.25	7.62	n.d	24.11	14.61	97.78
88		36.47	0.07	0.02	0.02	33.60	0.46	27.23	97.87	0.08	21.39	9.90	3.79	3.67	0.51	39.89	18.44	97.67
89		38.78	0.07	0.06	0.07	43.52	0.24	15.46	98.21	0.13	3.41	22.60	29.40	10.50	n.d	20.66	11.09	97.79
90		37.31	0.09	0.04	0.04	36.19	0.41	23.91	97.98	0.05	21.92	8.92	4.74	4.70	0.41	38.52	18.80	98.05
91		38.90	0.00	0.04	0.08	42.54	0.18	16.37	98.12	0.10	2.93	23.78	28.92	10.52	n.d	20.23	10.47	96.96
92		38.51	0.03	0.04	0.06	40.93	0.27	17.96	97.80	0.10	2.79	21.02	30.58	9.27	n.d	21.95	12.54	98.25
93		38.21	0.07	0.02	0.05	41.48	0.35	20.00	100.18	0.11	16.06	11.40	7.82	7.94	0.17	28.29	26.77	98.56
94		38.03	0.04	0.04	0.11	44.16	0.22	17.37	99.97	0.31	2.59	21.66	31.22	10.60	n.d	20.29	12.84	99.52
95		37.41	0.07	0.04	0.07	41.93	0.34	20.93	100.78	0.09	15.09	11.46	8.18	7.45	0.28	28.29	27.75	98.58
96		38.10	0.03	0.04	0.05	43.19	0.22	18.58	100.20	0.10	6.37	15.67	25.43	9.02	n.d	23.14	18.42	98.16
97		38.20	0.04	0.03	0.06	41.80	0.26	18.76	99.15	0.09	4.49	16.19	28.57	8.50	n.d	23.08	17.18	98.09
98		38.13	0.04	0.06	0.16	43.76	0.25	18.59	101.01	0.08	2.75	21.51	29.83	9.94	n.d	21.16	13.61	98.89
99		38.07	0.05	0.07	0.09	42.12	0.26	19.25	99.92	0.15	2.93	19.00	29.65	8.55	n.d	22.63	15.10	98.01
100		38.56	0.01	0.05	0.11	43.89	0.21	17.45	100.28	0.13	2.54	23.94	29.77	10.46	n.d	20.57	10.84	98.25
101		38.22	0.03	0.05	0.05	43.59	0.29	18.76	101.00	0.12	3.05	19.52	30.97	9.26	n.d	21.99	13.67	98.58
102		36.72	0.12	0.05	0.03	36.72	0.54	27.67	101.85	0.10	26.51	4.77	0.20	2.77	0.69	44.00	19.89	98.93
103		37.87	0.04	0.02	0.08	46.37	0.28	18.54	103.20	0.07	5.89	16.72	24.81	10.35	n.d	21.36	20.94	100.14
104		37.91	0.07	0.06	0.10	44.14	0.31	19.86	102.43	0.06	10.95	12.93	14.15	8.47	0.13	25.39	27.80	99.88

Tab. 1 (cont.)

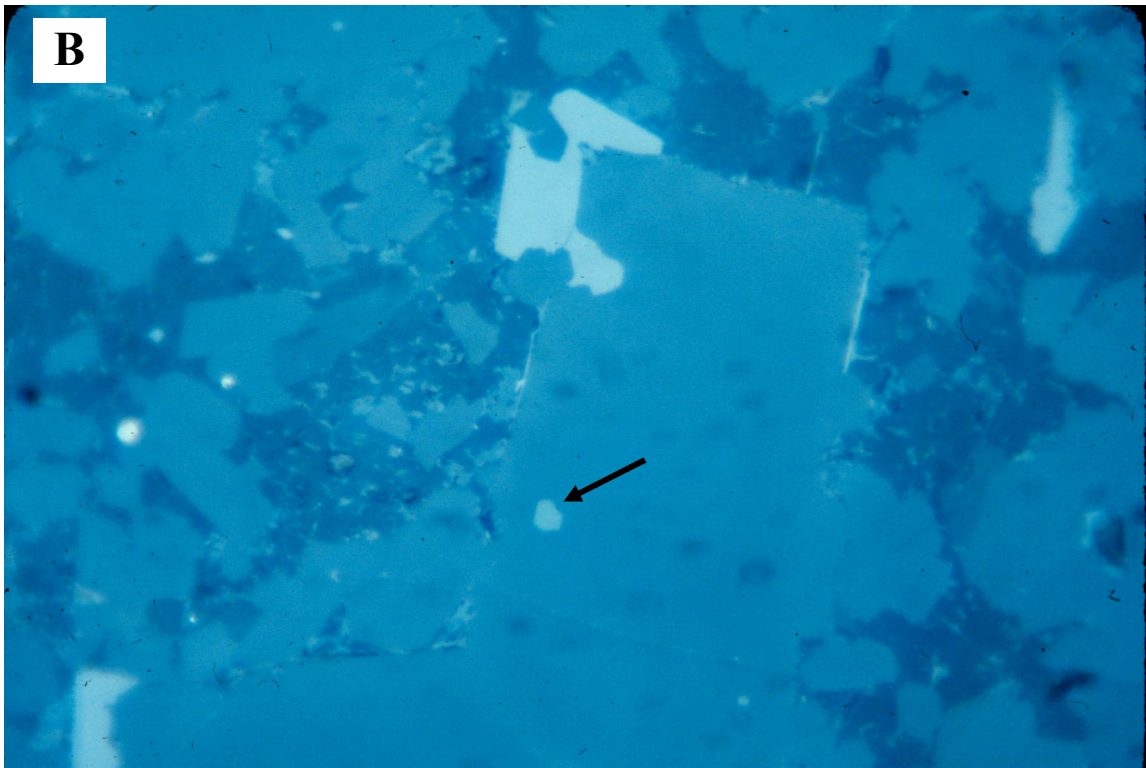
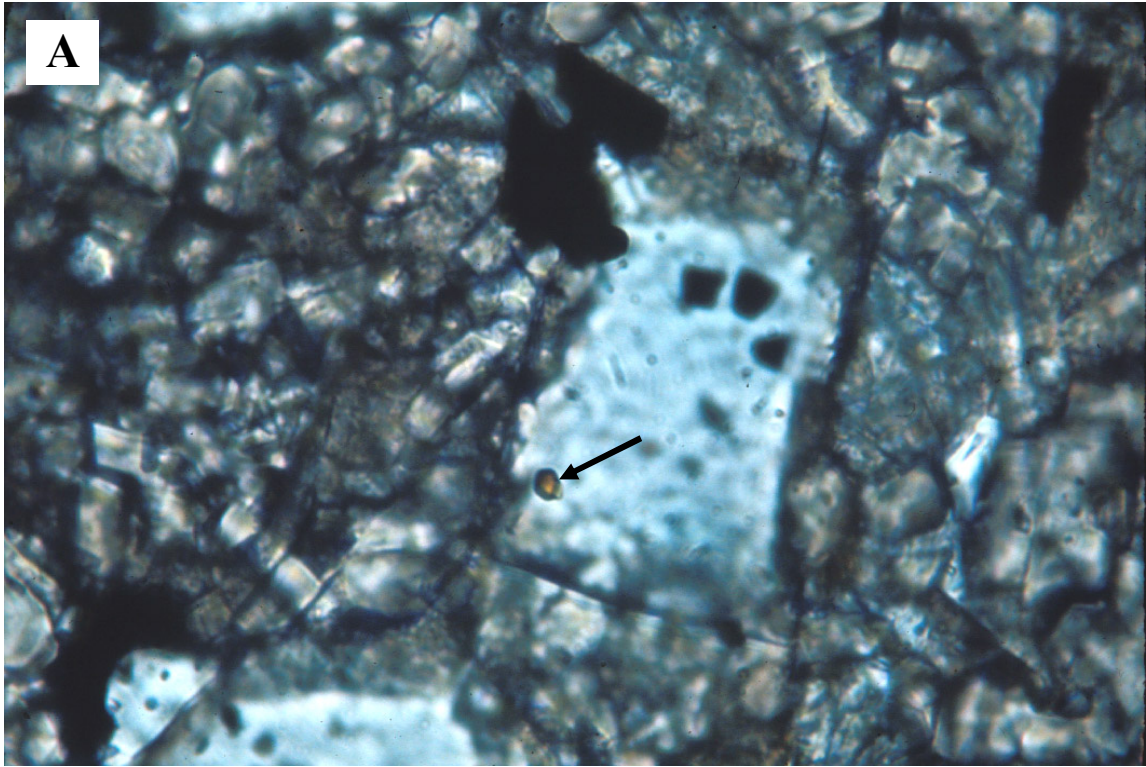


Fig. 1 – Spinel inclusions in olivine (black arrow). (A) transmitted light; (B) reflected light.

compositions, which otherwise would be lost by continuous reaction with the melt. Chemical data for spinel-olivine pairs have been collected analyzing spinel first and immediately after the olivine host 10 μm away from the spinel inclusion.

Spinel has six major components: Al_2O_3 , Cr_2O_3 , MgO , FeO , Fe_2O_3 and TiO_2 . TiO_2 content ranges from less than 2 wt. % up to 26 wt. % with increasing Fe/Mg. Spinel data are projected onto the Fe^{+3} - and Al^{+3} -free joins of the spinel compositional prism in Fig. 2a and 2b. These plots reveal distinctive general trends from early aluminous chromite to late titaniferous magnetite as expected.

Continuity in the trends displayed by spinels trapped in olivine suggest that spinel was indeed a stable phase throughout most the crystallization history of the basanite and therefore that it can potentially be used to estimate the temperature range of the crystallization interval. In this case any re-equilibration of Mg and Fe^{+2} that might have occurred between olivine and spinel during the cooling history is assumed to be negligible. Roeder et al. (1979) demonstrated that in fact this re-equilibration can take place in short intervals of time, from hours to weeks depending from re-equilibration temperature, and may seriously modify the Mg/ Fe^{+2} ratio in chromite. However, it is unlikely that olivine and spinel in the basanite re-equilibrated, due to the fact that the basanite contains glass in the matrix, which suggests at least rapid cooling if not quenching (Tracy, 1980).

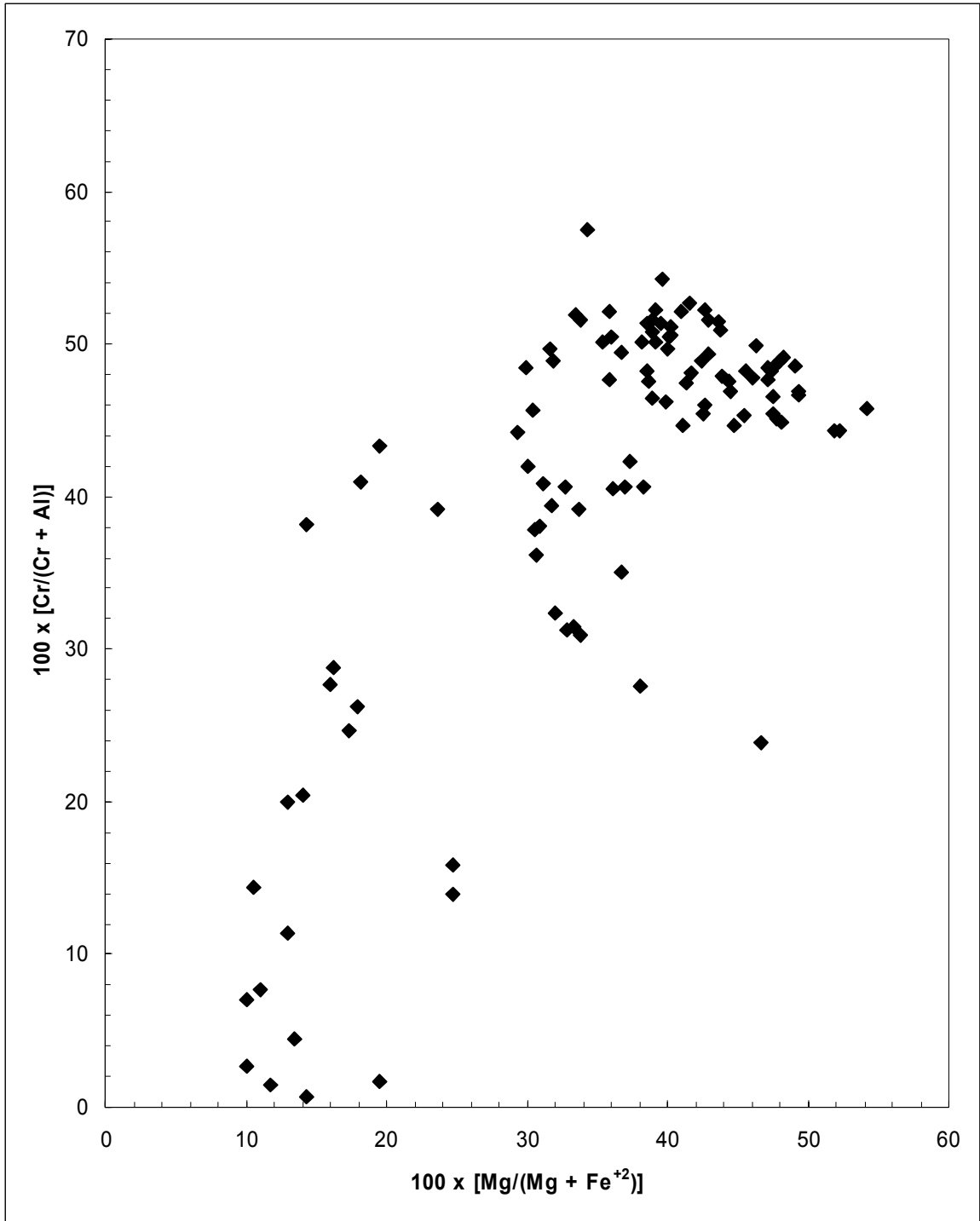


Fig. 2a – Mg/(Mg + Fe²⁺) vs Cr/(Cr + Al) plot for spinels inclusions in olivine.

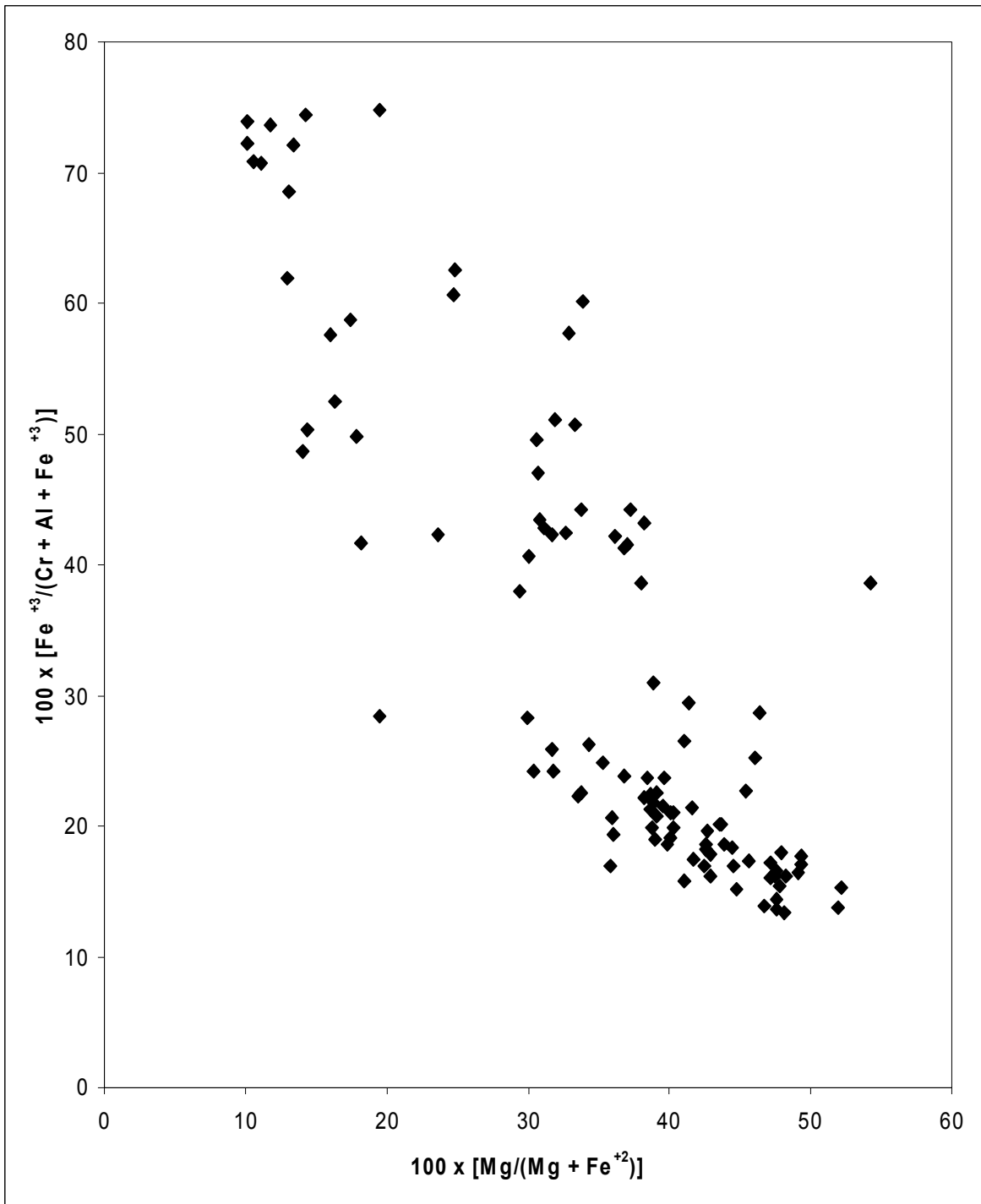


Fig. 2b – $\text{Mg}/(\text{Mg} + \text{Fe}^{+2})$ vs $\text{Fe}^{+3}/(\text{Cr} + \text{Al} + \text{Fe}^{+3})$ for spinel inclusions in olivine

Results.

Using olivine-spinel pair data as described above, we calculated equilibration temperatures using three different formulations of the olivine-spinel geothermometer: those of Roeder et al. (1979), Jianping et al. (1995) and Sack and Ghiorso (1991b).

Fig. 3 shows olivine-spinel temperatures calculated according to Roeder et al. (1979) plotted vs. $\text{Cr}/(\text{Cr} + \text{Al} + \text{Fe}^{+3})$ in spinel. While a clear relationship exists, as expected, between Cr content and recorded temperatures, it is apparent that one data cluster defines temperatures from ~ 800 to 1200 °C over a limited range of Cr content and a second linear trend departs from the cluster at $\sim \text{Cr}/(\text{Cr} + \text{Al} + \text{Fe}^{+3}) = 0.35$ and defines temperatures that decrease from ~ 1000 °C to < 400 °C.

Fig. 4 shows temperatures calculated according to Jianping et al. (1995) also plotted vs. $\text{Cr}/(\text{Cr} + \text{Al} + \text{Fe}^{+3})$. A pattern very similar to that of Fig. 3 is obvious, with one data cluster defining a temperature range from ~ 1000 to 1300 °C at high Cr content and a linear trend departing from the cluster at $\sim \text{Cr}/(\text{Cr} + \text{Al} + \text{Fe}^{+3}) = 0.35$ defining temperatures gradually decreasing from ~ 1100 °C to < 600 °C.

Fig 5 shows temperatures calculated according to Sack and Ghiorso (1991b) plotted vs. $\text{Cr}/(\text{Cr} + \text{Al} + \text{Fe}^{+3})$. The pattern displayed, albeit similar to those in Fig. 3 and 4, shows some differences. The high temperature cluster spans a range from ~ 950 °C to ~ 1200 °C, whereas the trend defining decreasing temperatures is much less distinct and data spread over a range from ~ 1000 °C to ~ 650 °C.

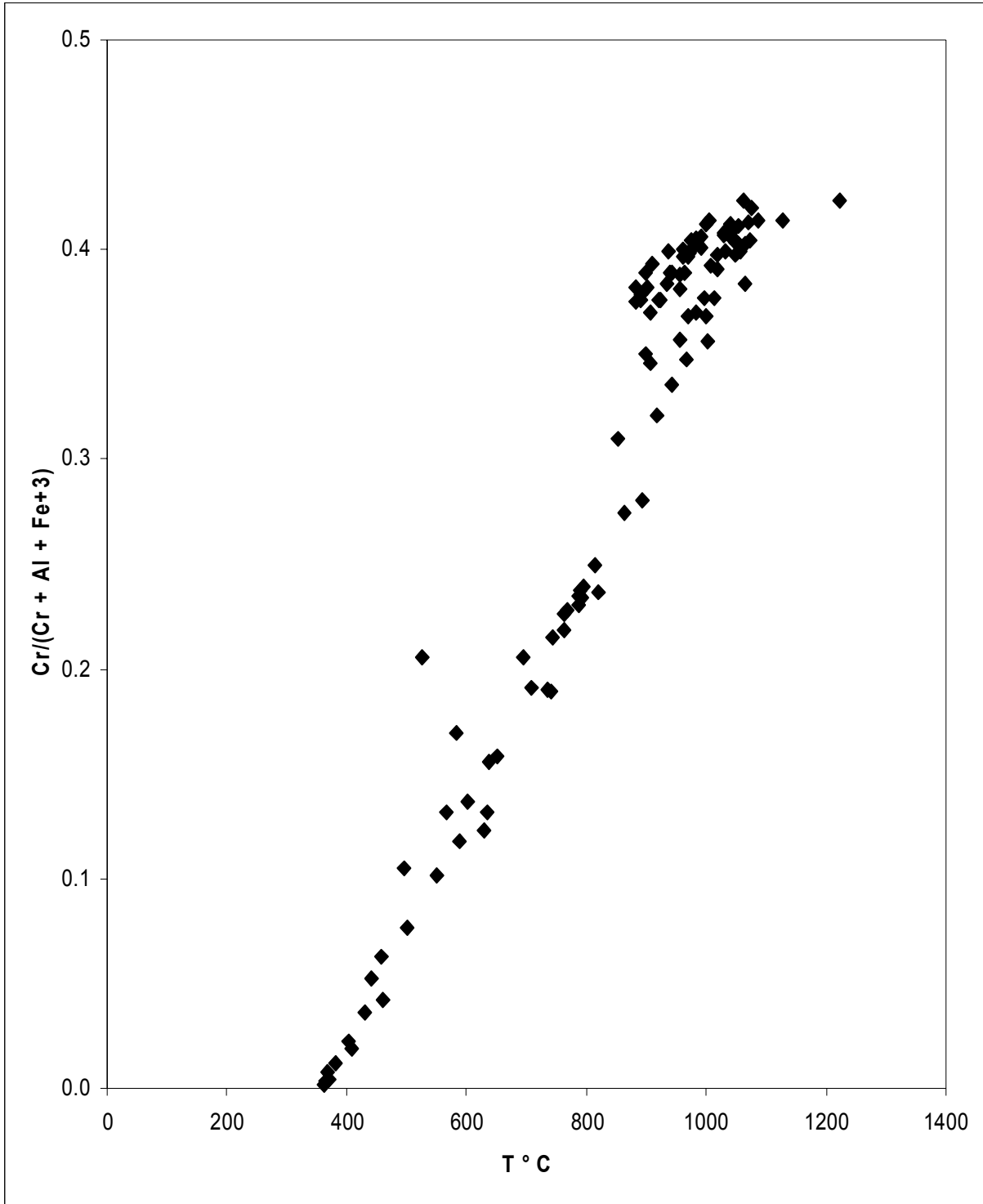


Fig. 3 - Temperatures calculated according to Roeder et al. (1979) plotted vs. $\text{Cr}/(\text{Cr} + \text{Al} + \text{Fe}^{+3})$ in spinel.

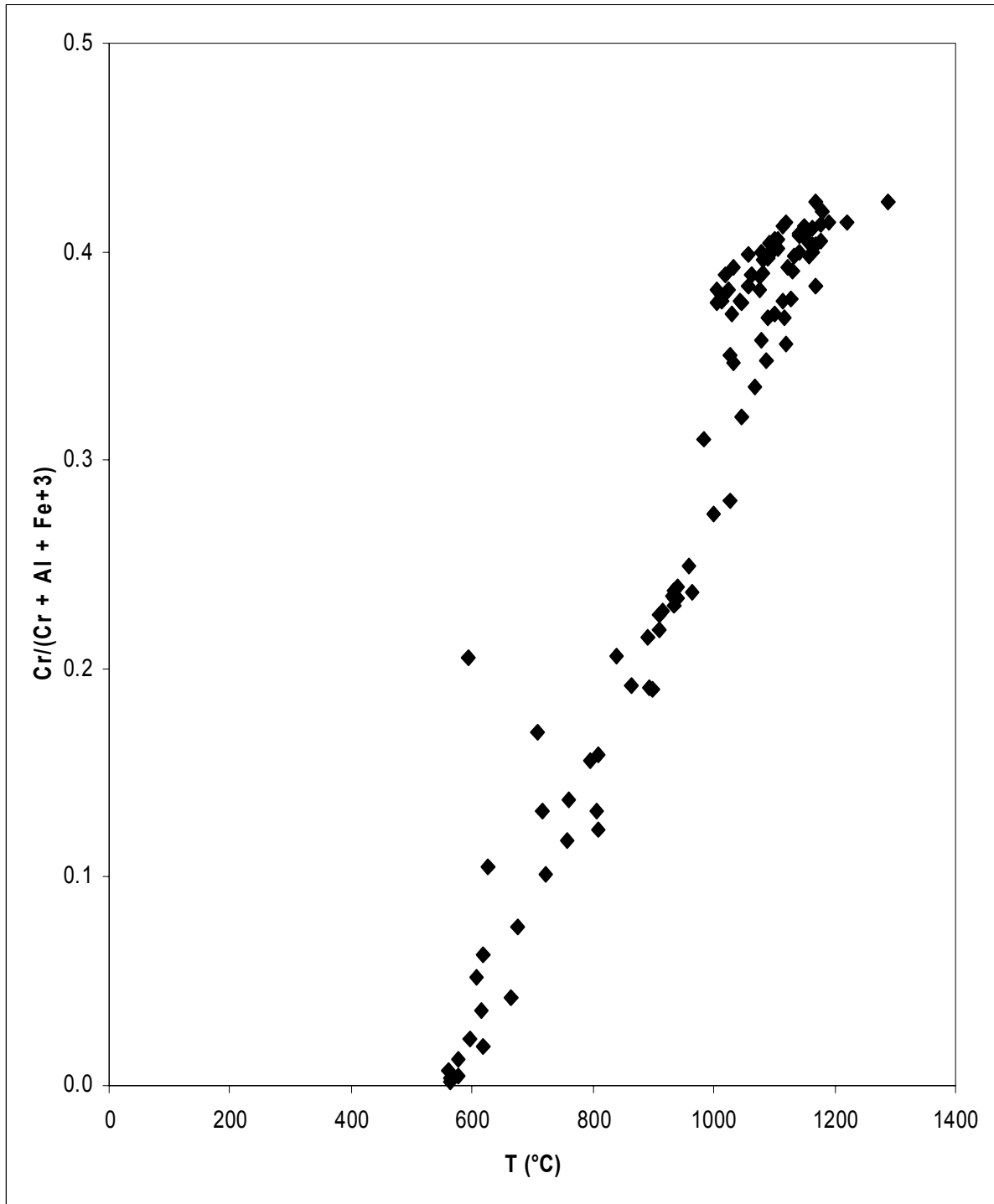


Fig. 4 – Temperatures calculated according to Jianping et al. (1995) plotted vs. $\text{Cr}/(\text{Cr} + \text{Al} + \text{Fe}^{+3})$.

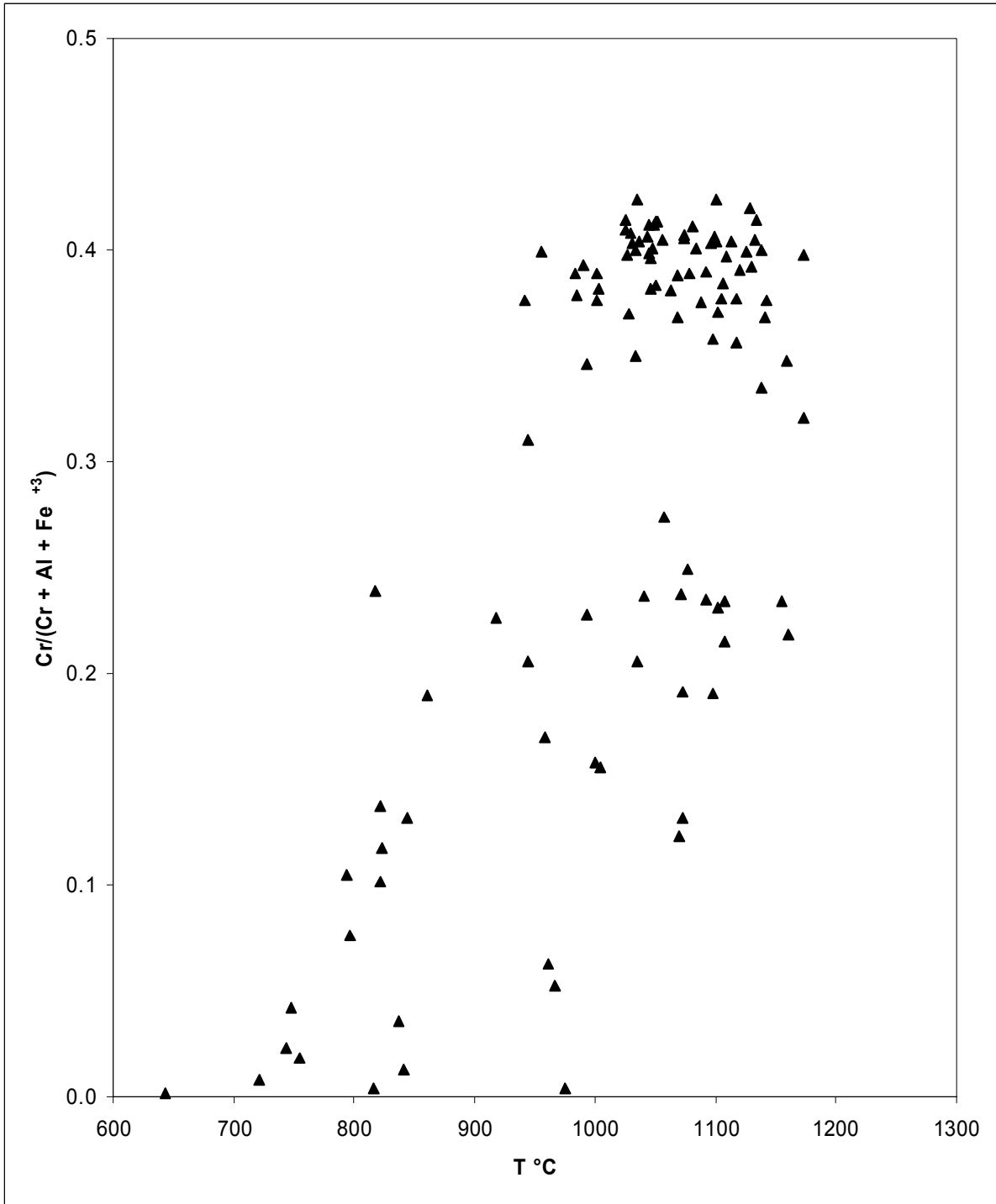


Fig. 5 – Temperatures calculated according to Sack and Ghiorso (1991b) plotted vs. $\text{Cr}/(\text{Cr} + \text{Al} + \text{Fe}^{+3})$.

Discussion.

We can estimate a temperature range for the thermal evolution of the Tahiti basanite independently from the olivine-spinel thermometer. The source region for the basanite can be set at the intersection between a mantle-plume adiabat and the dry peridotite solidus (Green, 1973). Class and Goldstein, 1997 proposed a mantle-plume adiabat ~ 300 °C above the asthenospheric adiabat of McKenzie and Bickle, 1988, which would set the upper limit for the basanite at ~ 1500 °C (Fig. 6). Tracy and Stolper, based on experiments at 1 Atm on the Tahiti basanite suggest a solidus temperature of 1350 °C (unpublished data, Fig. 6).

A lower temperature limit for the crystallization of the basanite can be estimated using the ilmenite and spinel pair in the groundmass. We analyzed ilmenite and magnetite in the basanite ground mass (maximum distance between ilmenite and spinel ~ 50 μm) and calculated equilibration temperatures using the software QUILF, which incorporates the solution model defined by Andersen and Lindsley (1988). Calculated temperatures range from 726 to 818 °C (Tab. 2), which agree with our previous statement that low temperatures calculated with the olivine-spinel thermometer are unrealistic.

Spinel-olivine geothermometer calibrations are based on specific assumptions regarding the type of solid solution model for both olivine and spinel. These assumptions may presume complete ideality (e.g., Irvine, 1965) or use more sophisticated solid solution theory and restrict assumptions to ordering of cations in crystal sites (Sack and Ghiorso, 1991b). Although ideality is a reasonable assumption for olivine at high temperature (Bradley, 1962; Nafziger and Muan, 1967), it is an acceptable but not necessarily realistic hypothesis for spinels (Irvine, 1965; Sack

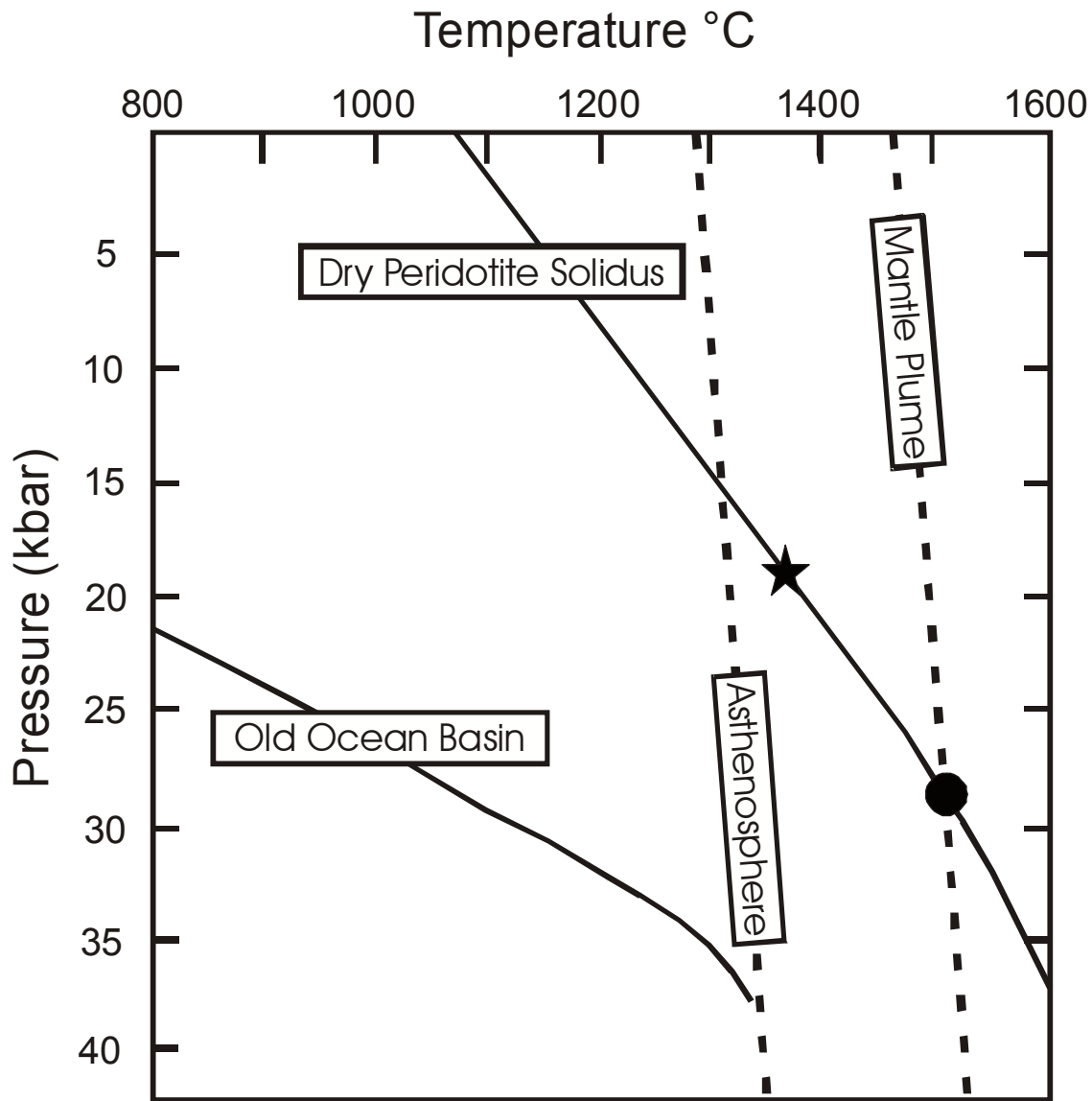


Fig. 6 – Pressure-temperature diagram showing a possible range for formation conditions of the Tahiti basanite: **black dot** – lower P-T limit based on mantle plume adiabat and dry peridotite solidus; **star** – upper P-T limit based on dry peridotite solidus and liquidus temperature for the Tahiti basanite (~ 1350 °C, Tracy and Stolper, unpublished data). Mantle Plume adiabat from Class and Goldstein (1997), asthenosphere adiabat from McKenzie and Bickle (1988), Dry Peridotite Solidus from Green (1973) and Old Ocean Basin adiabat from Class and Goldstein, 1997.

	SiO2	TiO2	Al2O3	Cr2O3	MnO	MgO	FeO	Fe2O3	TOTAL	T (°C)
Magnetite	0.08	26.25	4.22	0.04	0.68	3.06	42.77	22.15	99.25	771
Ilmenite	0.32	50.10	0.16	n.d.	0.95	1.23	41.90	3.49	98.15	
Magnetite	0.23	26.41	4.77	0.14	0.58	4.38	40.72	21.37	98.60	784
Ilmenite	0.06	50.63	0.14	n.d.	0.99	1.50	41.85	3.36	98.54	
Magnetite	0.09	26.71	3.94	0.05	0.71	3.04	43.18	21.01	98.73	818
Ilmenite	0.11	50.19	0.11	n.d.	0.92	1.87	40.87	3.71	97.78	
Magnetite	0.05	26.17	5.24	0.13	0.70	3.83	41.84	21.92	99.88	760
Ilmenite	0.68	49.21	0.31	n.d.	1.15	0.85	41.57	4.02	97.79	
Magnetite	0.44	26.44	4.35	0.20	0.65	3.61	42.06	21.58	99.33	726
Ilmenite	0.08	49.81	0.05	n.d.	1.25	0.57	42.51	3.58	97.85	
Magnetite	0.05	26.65	4.23	0.03	0.66	3.22	43.13	22.20	100.16	799
Ilmenite	0.09	49.85	0.06	n.d.	0.90	1.28	41.63	3.84	97.65	

Tab. 2. Ilmenite-magnetite analyses and temperatures calculated with QUILF (Andersen and Lindsley, 1988)

and Ghiorso, 1991b). According to Irvine (1965) “chemical data on olivine and spinel formed together in equilibrium at a temperature where both phases behaved as ideal solutions should define a planar surface in a rectilinear 3-dimensional plot” of:

$$X = \ln K_D; \quad Y = Y_{Cr}^{sp}; \quad Z = Y_{Fe^{+3}}^{sp}$$

This plot is shown in Fig. 7 for data of this study and reveals a linear relationship among the three parameters. It also shows that high-Cr and low-Fe⁺³ spinels seem to depart to some extent from the planar surface, suggesting that an assumption of ideality might not be totally correct for those compositions. For this reason we chose to evaluate our data using various formulations of the olivine-spinel geothermometer in which different thermodynamic models are used for the spinel solid solution.

Temperature ranges calculated using the three different geothermometers agree reasonably well for the high-Cr spinel cluster [i.e. data with $Cr/(Cr + Al + Fe^{+3}) \geq 0.35$; Fig. 3, 4, 5]. However the linear trends displayed in Fig. 3 and 4 extend toward temperatures that are obviously unrealistically low for olivine and spinel crystallization and in addition the trend in Fig. 5 shows a wide dispersion.

Our data on olivine-spinel pairs record decreasing temperatures during the crystallization history of the magma, as expected. The trends indicated by the Roeder et al. (1979) and Jianping et al. (1995) thermometers could be ascribed to the presence of Ti in spinel, which is not considered in these two formulations and may be responsible for the unrealistically low calculated temperatures. Indeed TiO₂ in our spinels ranges from 1.8 to 26.5 wt. % and the Ti content increases strongly with decreasing Cr content (Fig. 8).

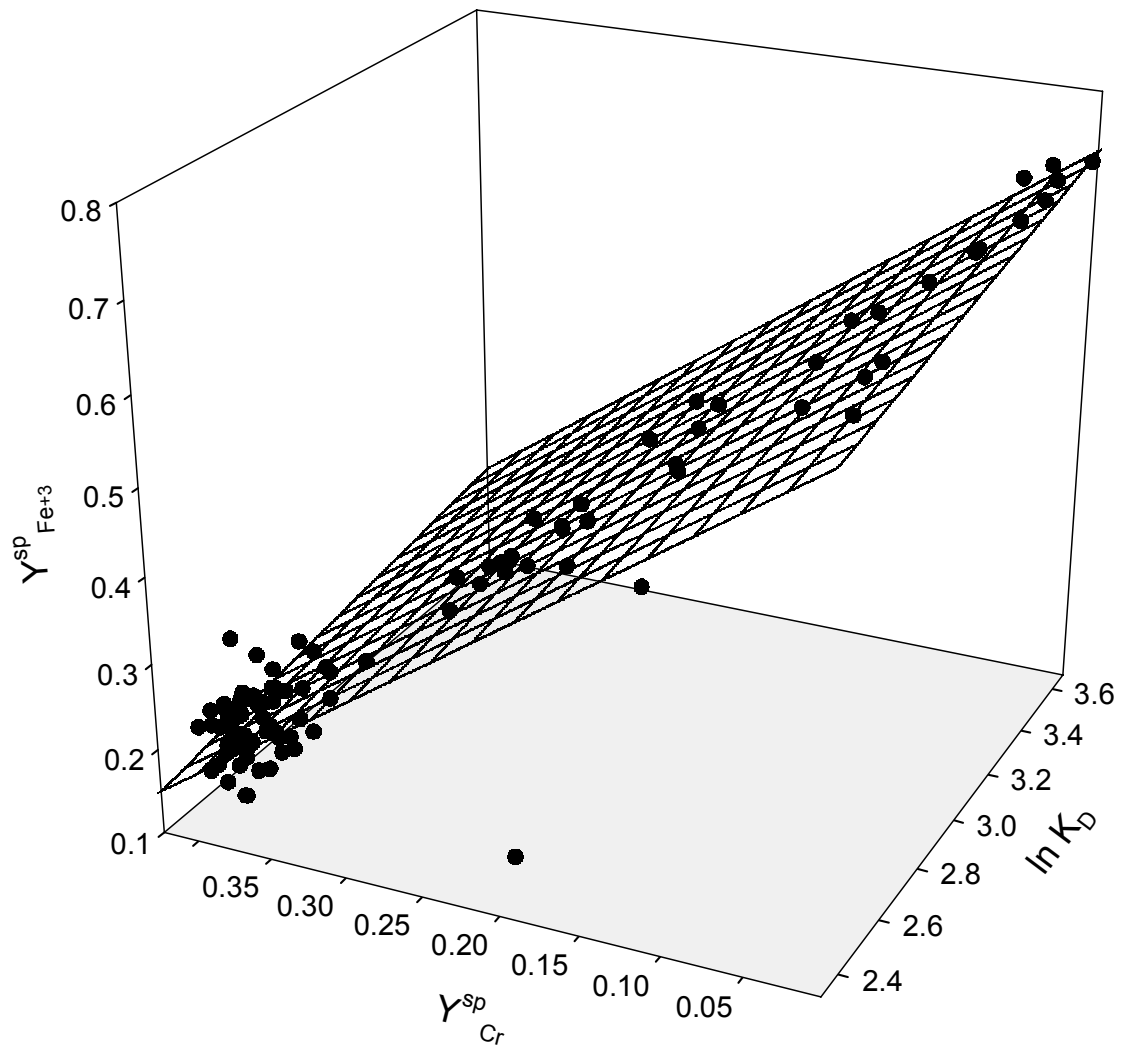


Fig. 7 – 3-dimensional plot [$\ln K_D$ vs. Y_{Cr}^{sp} vs. $Y_{Fe^{+3}}^{sp}$] for spinel and olivine data (see text for discussion).

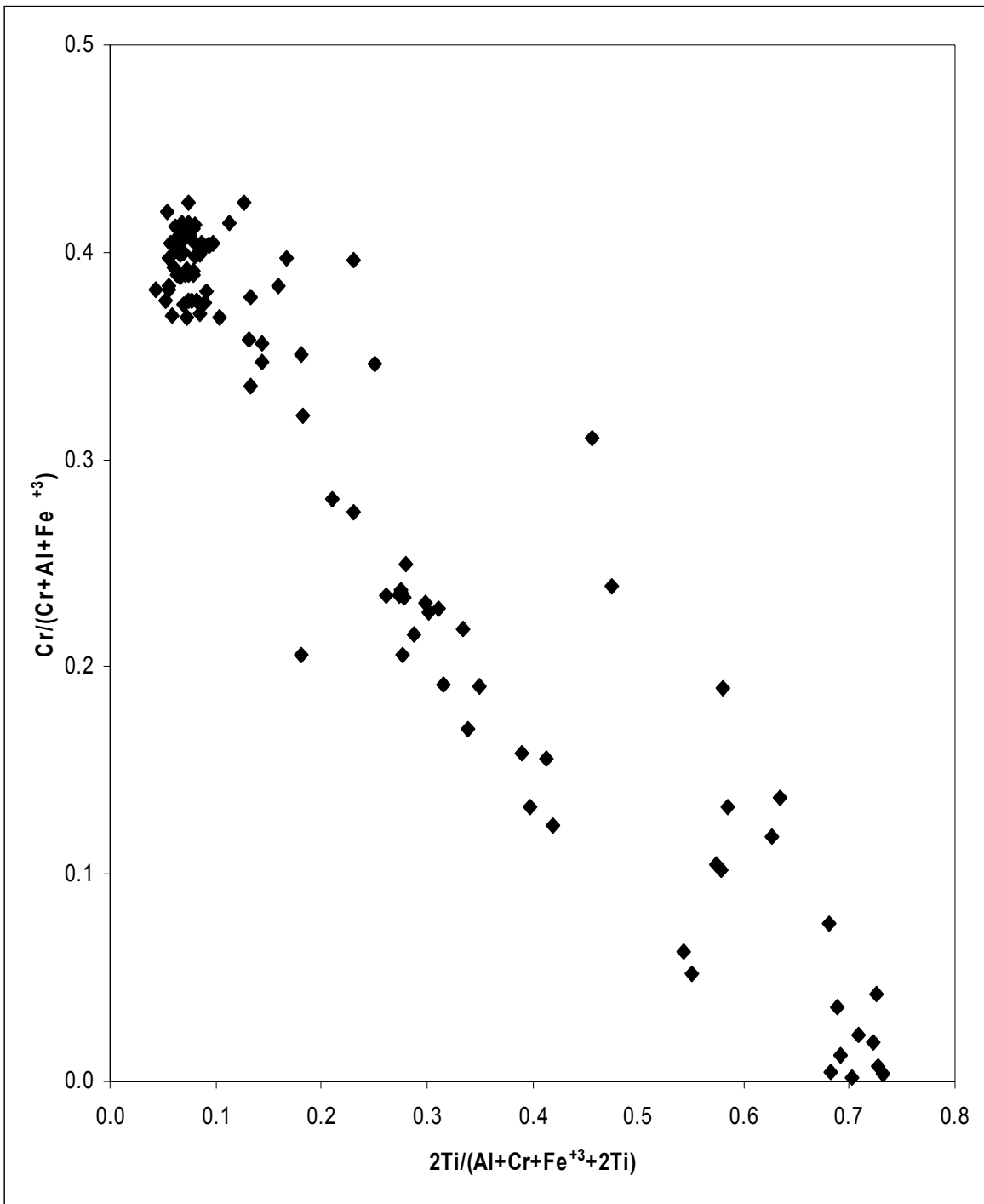


Fig. 8 – Relationship between Ti and Cr content in spinels.

Ti⁴ preferentially occupies octahedral sites in spinels (site B), which it shares with Fe⁺³. In the case of extensive solid solution toward ulvospinel (Fe₂TiO₄) end-member, the Mg/Fe⁺² ratio in the spinel will be strongly decreased due to the two following exchange reactions:



Both exchanges strongly favor Fe over Mg as the divalent cation (Mg is almost absent in natural magnetite and ulvospinel components). The presence of Ti in the octahedral site (VI) forces additional Fe⁺² into the spinel structure (since Fe⁺² + Ti substitutes for 2Cr) and likely also affects the Fe⁺² content in the tetrahedral site (IV).

The practical effect with geothermometers calibrated for Cr-rich spinels, and that do not take into account the presence of Ti, would be an overestimation of K_D for the olivine-spinel pair, which in turn results in lower calculated temperatures.

A possible way to account for this effect is to subtract Ti from the total Fe⁺² (on a formula basis). In this case we have two possibilities:

- 1) assuming that the presence of Ti affects only the Fe⁺² content in the octahedral site and applying the correction: Fe⁺² - Ti;
- 2) assuming that the presence of Ti affects not only the Fe⁺² content in the octahedral site, but also the Fe⁺² content in the tetrahedral site and applying the correction: Fe⁺² - 2Ti (albeit this is likely to overcorrect).

As a test we applied these empirical corrections to the Roeder et al. (1979) thermometer. Fig. 9 [9a correction (1) and 9b correction (2)] display the temperatures calculated after the corrections according to the Roeder et al. (1979) thermometer. The corrections produced higher

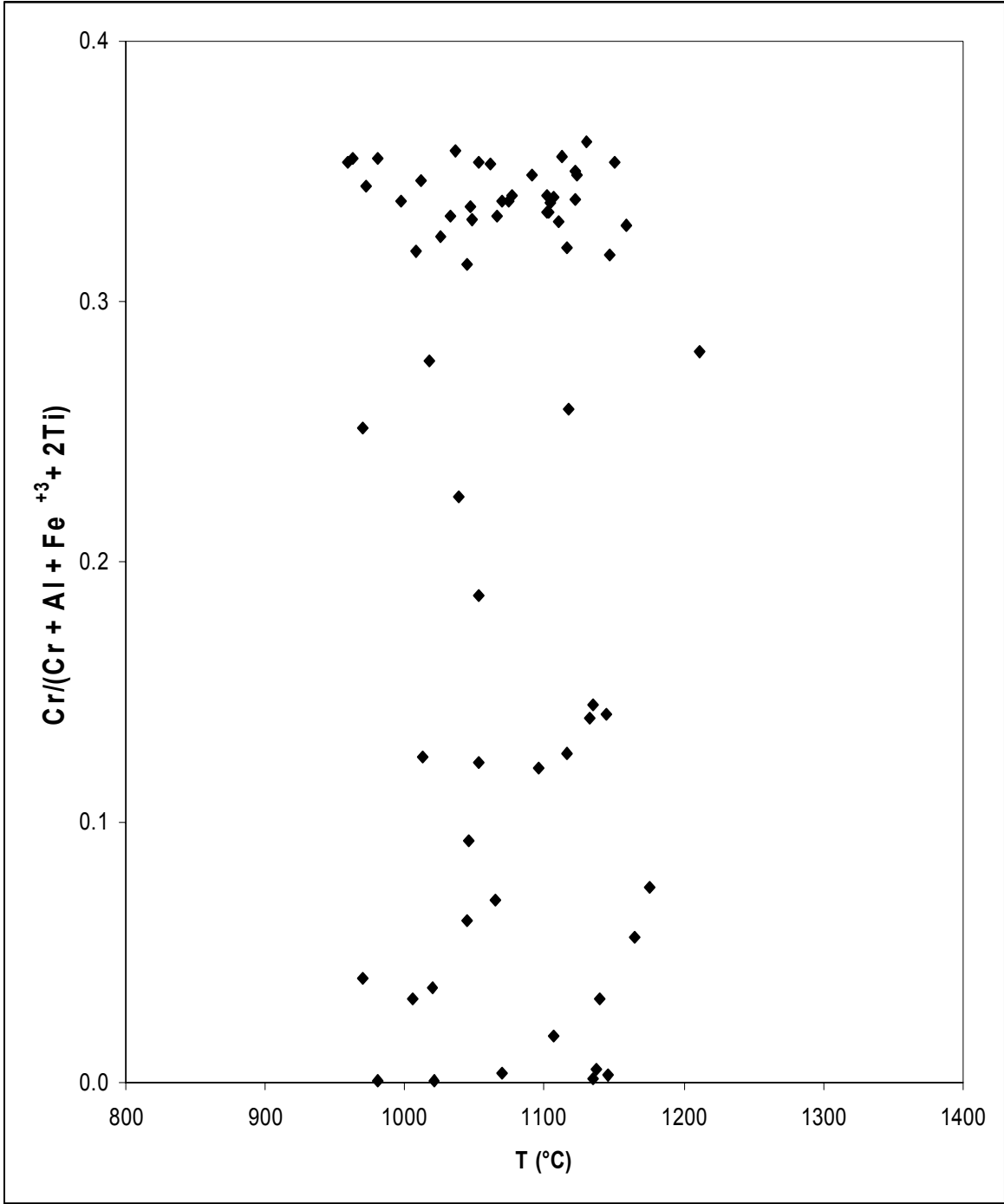


Fig. 9a - Temperatures calculated according to Roeder et al. (1979) after correction (1) for Ti content (see text for discussion).

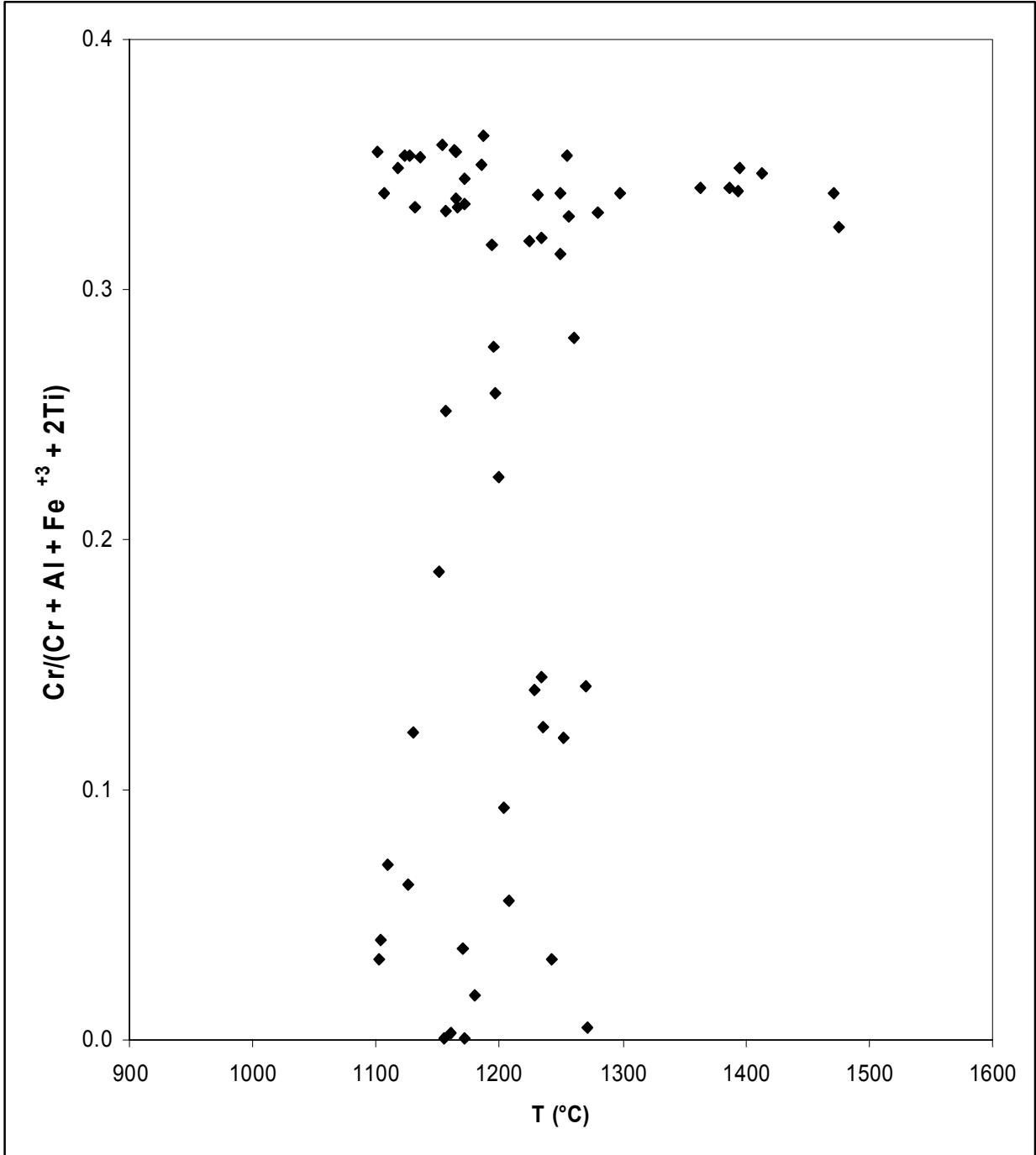


Fig. 9b – Temperatures calculated according to Roeder et al. (1979) after the correction (2) for Ti content (see text for discussion).

temperatures both in the high-T cluster and in the linear trend but it also generated a major dispersion in the data (Fig. 7). When correction (1) is applied (Fig. 9a), the range of the calculated temperatures is very realistic (from < 1300 to > 900 °C). These results support our interpretation that high Ti content is responsible for the anomalous uncorrected calculated temperatures, but at the same time the dispersion of the data indicates that the real situation is more complex. A simple linear correction is probably not completely appropriate since the behavior (i.e. site occupancy) of other elements may very well be affected by the presence of Ti (Mg in tetrahedral site for instance, through the contribution of Mg_2TiO_4 end-member).

The calibration by Sack and Ghiorso (1991) produces temperatures similar to those obtained with the other two calibrations, but the larger dispersion of the data for the linear trend (Fig. 5) indicates the problems that even this model has with Ti-rich spinels. Indeed Sack and Ghiorso (1991) pointed out that they did not consider the contribution of the short-range cation ordering to the configurational entropy for titanate spinels and this could produce errors in evaluating data from Ti-bearing spinels from petrologic systems.

Conclusions.

Using three different calibrations of the olivine-spinel geothermometer we evaluated the range of magmatic temperatures within the crystallization interval for a basanite. Results are consistent between the three geothermometers. However while the olivine-spinel pair undoubtedly records the thermal evolution of the basanite magma during crystallization, the low temperatures calculated with all the three geothermometers are unrealistic especially when compared with temperatures calculated according to the ilmenite-spinel thermometer (Tab. 2). This is likely due

to the presence of significant amounts of the ulvospinel end-member in the most fractionated magmatic spinels. Indeed the role of Ti is not taken into account in two of the geothermometers (Roeder et al., 1979; Jianping et al., 1995) or is not fully accounted for in the spinel solid solution model (Sack and Ghiorso, 1991).

We tested the possibility a simple correction for the presence and effects of Ti by applying a linear correction to the Fe^{+2} content in our spinels. While this generated more realistic temperatures at the low end of the range, it also increased the dispersion in the data, suggesting that spinel behavior is more complex and that possibly the presence and site occupancy of other elements besides Fe^{+2} may very well be affected by the presence of Ti.

References

- Andersen D.J. and Lindsley D.H. (1988) Internally consistent solution models for Fe-Mg-Mn-Ti oxides; Fe-Ti oxides. *American Mineralogist*, vol.73, no.7-8, pp.714-726.
- Bradley R.S. (1962) Thermodynamic calculations on phase equilibria involving fused salts. Part II. Solid solutions and applications to olivines. *Am. J. Sci.* 260 (7):550-554.
- Class C. and Goldstein S.L. (1997) Plume-lithosphere interactions in the ocean basins: constraints from the source mineralogy. *EPSL*, 150:245-260.
- Evans B.W. and Wright T.L. (1972) Compositions of liquidus chromite from the 1959 (Kilauea Iki) and 1965 (Makaopuhii) eruptions of the Kilauea volcano. *Am. Mineral.* 57:217-230.
- Green D.H. (1973) Conditions of melting of basanite magma from garnet peridotite. *EPSL*, 17:456-465.
- Irvine T.N. (1965) Chromian Spinel as a Petrogenetic Indicator: part 1. Theory. *Can. J. Earth Sc.* 2:648-672.
- Jackson E.D. (1969) Chemical variation in coexisting chromite and olivine in the chromitite zones of the Stillwater complex. *Econ. Geol. Mon.* 4:41-71.
- Jianping L., Kornprobst J., Vielzeuf D. and Fabries J. (1995) An Improved Experimental Calibration of the Olivine-Spinel Geothermometer. *Chin. J. Geochem.* 14 (1):68-77.
- McBirney A.R. and Aoki K. (1968) Petrology of the island of Tahiti. In R.R. Coats, R.L. Hay and C.A. Anderson Eds. *Studies in Volcanology: A Memoir in Honor of Howell Williams*, Geol. Soc. Am. Mem., 116:523-556.
- McKenzie D. and Bickle M.J. (1988) The volume and composition of melt generated by extension of the lithosphere. *J. Petrol.* 29:625-679.
- Nafziger R.H. and Muan A. (1967) Equilibrium phase compositions and thermodynamic properties of olivines and pyroxenes in the system MgO-“FeO”-SiO₂ *Am. Mineral.* 52:1364-1386.

- Roeder P.L., Campbell I.H. and Jamieson H.E. (1979) A Re-Evaluation of the Olivine-Spinel Geothermometer. *Contrib. Mineral. Petrol.* 68:325-334.
- Sack R.O. and Ghiorso M.S. (1991a) An internally consistent model for the thermodynamic properties of Fe-Mg-titanomagnetite-aluminate spinels. *Contrib. Mineral. Petrol.* 106:474-505.
- Sack R.O. and Ghiorso M.S. (1991b) Chromian spinels as petrogenetic indicators: Thermodynamics and Petrological applications. *Am. Mineral.* 76:827-847.
- Tracy R.J. (1980) Petrology and Genetic Significance of an Ultramafic Xenolith Suite from Tahiti. *EPSL* 48:80-96.
- Tracy R.J. and Robinson P. (1977) Zoned titanian augite in alkali olivine basalt from Tahiti and the nature of titanium substitution in augite. *Am. Mineral.* 62:634-645.
- Wood B.J. and Nicholls J. (1978) The thermodynamic properties of reciprocal solid solutions. *Contrib. Mineral. Petrol.* 66:389-400.

VITA

Luca Fedele was born on May 30th 1964 in Naples, Italy. After receiving his Laurea he moved to the United States to get a PhD in Geology. Now that the PhD has been completed he is going back to Naples to pursue a career in the Italian University.

Luca Fedele